

Deep Spectroscopy of Systematically Surveyed Extended Lyman- α Sources at $z \sim 3 - 5$ ¹²

Tomoki Saito^{3,4}, Kazuhiro Shimasaku³, Sadanori Okamura³, Masami Ouchi^{5,6}, Masayuki Akiyama⁷, Michitoshi Yoshida⁸, Yoshihiro Ueda⁹

ABSTRACT

Spatially extended Ly α sources that are faint and/or compact in continuum are candidates for extremely young ($\lesssim 10^7$ yrs) galaxies at high redshifts. We present medium-resolution ($R \sim 2000$) spectroscopy of such extended Ly α sources found in our previous study at $z \sim 3 - 5$, using VLT/VIMOS. The deep spectroscopy showed that all 18 objects we observed have large equivalent widths (EWs) exceeding 100Å. For about 30% of our sample (five objects), we identified conspicuous asymmetry on the profiles of the Ly α line. They show broad wing emission components on the red side, and sharp cut-off on the blue side of the Ly α line. Such asymmetry is often seen in superwind galaxies known to date, and also consistent with a theoretical prediction of superwinds. In fact, one of them show systematic velocity structure on the 2-dimensional spectrum suggesting the existence of superwind activity. There are eight objects (8/18 \sim 40%) that have large EWs exceeding 200Å, and no clear signature of superwind activities. Such large EWs cannot be explained in terms of photo-ionization by a moderately old ($> 10^7$ yrs) stellar population, even with a top-heavy IMF or an extremely low metallicity. These eight objects clearly show a positive correlation between the Ly α line luminosity and the velocity width. This suggests that these eight objects are good candidates for forming-galaxies in a gas-cooling phase.

Subject headings: galaxies:formation — galaxies:high redshift

³Department of Astronomy, University of Tokyo, 7-3-1 Hongo, Bunkyo, Tokyo 113-0033, Japan

⁴Present Address: Dark Cosmology Centre, Niels Bohr Institute, University of Copenhagen, Juliane Maries Vej 30, 2100 Copenhagen Ø, Denmark, e-mail: tomoki@dark-cosmology.dk

⁵Space Telescope Science Institute, 3700 San Martin Drive, Baltimore, MD 21210, USA

⁶Hubble Fellow

⁷Subaru Telescope, National Astronomical Observatory of Japan, North A'ohoku Place, Hilo, HI 96720, USA

⁸Okayama Astrophysical Observatory, National Astronomical Observatory of Japan

⁹Department of Astronomy, Kyoto University, Sakyo-ku, Kyoto 606-8502, Japan

1. Introduction

Galaxies undergoing their initial star formation are predicted to have strong Ly α emission (Partridge & Peebles 1957; Charlot & Fall 1993). Recent imaging surveys using narrowband filters tuned to the redshifted Ly α line have successfully identified a large number of Ly α emitters (LAEs, e.g. Cowie & Hu 1998; Hu et al. 1998; Fynbo et al. 2001, 2003; Rhoads et al. 2000, 2003; Ouchi et al. 2003, 2005; Shimasaku et al. 2003; Kodaira et al. 2003; Maier et al. 2003; Dawson et al. 2004; Kashikawa et al. 2005; Iye et al. 2006). Some of them are fairly faint in rest-frame UV continuum and have large Ly α equivalent widths exceeding 240Å (Malhotra & Rhoads 2002, hereafter MR02). Such large equivalent widths suggest that they are possibly in the initial phases ($\ll 10^7$ yrs) of star formation. The faintness in UV continuum also suggests that their stellar masses are fairly small, implying that a significant star formation has not yet occurred.

In such early phases of galaxy formation (age of $\lesssim 10^7$ yrs), (proto)galaxies are predicted to radiate spatially extended Ly α emissions. At least three mechanisms are currently proposed for extended Ly α emissions; *i*) cooling radiation from gravitationally heated primordial gas infalling into a dark halo potential (Haiman et al. 2000; Fardal et al. 2001; Furlanetto et al. 2004; Birnboim & Dekel 2003; Dekel & Birnboim 2006; Dijkstra et al. 2006a,b), *ii*) resonant scattering of Ly α photons from the central (hidden) ionizing source (Møller & Warren 1998; Haiman & Rees 2001; Weidinger et al. 2004, 2005; Laursen & Sommer-Larsen 2006), *iii*) starburst-driven galactic winds (Taniguchi & Shioya 2000; Taniguchi et al. 2001; Ohyama et al. 2003; Geach et al. 2005).

Recent narrowband imaging surveys for high- z Ly α emitters (LAEs) have found several tens of extended Ly α sources with no significant UV continuum sources sufficient to ionize such a large amount of H I gas (Ly α blobs, or LABs: Keel et al. 1999; Steidel et al. 2000; Francis et al. 2001; Matsuda et al. 2004; Palunas et al. 2004; Dey et al. 2005; Nilsson et al. 2006). However, there are still only restricted number of extended Ly α sources known to date, while thousands of normal LAEs are already known. Most of the extended Ly α sources known to date are identified in narrowband imaging surveys, which cover very narrow redshift range. Even the largest sample made by Matsuda et al. (hereafter M04), which is constructed from a narrowband survey targeted on LABs of Steidel et al. (2000, hereafter S00), covers a redshift range of only $z = 3.06^{+0.04}_{-0.03}$.

Due to the lack of a systematic sample and subsequent follow-up studies, nature of such extended Ly α sources remains unknown. Even for the most famous objects, two LABs of S00, the origins of the extended Ly α emission are not fully clear. For example, observational studies of S00's LABs are made by many astronomers, ranging from radio to X-ray wavelengths (e.g. Chapman et al. 2001, 2004; Basu-Zych & Scharf 2004; Geach et al. 2005; Matsuda et al. 2006). These studies suggest that obscured ionizing sources such as starburst regions or AGNs are as-

¹Based on observations made with ESO telescope at the Paranal Observatory, under the programme ID 074.A-0524

²Based on data collected at the Subaru Telescope, which is operated by the National Astronomical Observatory of Japan.

sociated with LABs. Detailed optical spectroscopy of the LABs suggests that outflow from the central sources are responsible for the extended Ly α emission (Ohyama et al. 2003; Wilman et al. 2005), while numerical simulation shows that cooling radiation from infalling gas combined with a central ionizing source can also explain the spatial extent, line profiles, and velocity widths of the Ly α emission (Dijkstra et al. 2006b). There is also a detailed observational study by Bower et al. (2004) suggesting that extended Ly α emission of LAB cannot be simply explained with a single mechanism such as a galactic wind or cooling radiation. They are likely to be massive systems harboring galaxy formation sites (Matsuda et al. 2006), although the true nature of the Ly α emission are still unclear.

In order to construct a systematic sample of extended Ly α sources covering a wide range of redshift, we have carried out a deep, wide-field imaging survey of a blank-field, Subaru/*XMM-Newton* Deep Field, using Subaru Telescope and seven intermediate-band (IA) filters. This survey enabled us to construct a sample of 41 extended Ly α sources located at $z \sim 3 - 5$, and also to show that this kind of objects commonly exist in the early universe far beyond $z \sim 3$ (Saito et al. 2006, hereafter Paper1). We here present a deep follow-up spectroscopy of our photometric sample of Paper1 using high-resolution grism of VIMOS on VLT. This gives a three times deeper exposure and a several times higher resolution than our previous spectroscopy presented in Paper1. We constructed a spectroscopic sample of 18 spatially extended Ly α sources with large equivalent widths, located at redshifts of $3.3 \lesssim z \lesssim 4.7$. This sample allows us to make a quantitative analysis in terms of equivalent width, velocity width, and Ly α line luminosity, as well as the velocity structure traced by the Ly α line profile.

The rest of this paper is organized as follows. We briefly introduce our photometrically selected sample of extended Ly α sources in §2, based on the previous observations in Paper1. In §3 we present the details of our spectroscopic observations and data reduction. The results of the spectroscopy thus obtained and a discussion based on them are presented in §4. Finally, we summarize the conclusions in §5.

All magnitudes are in the AB (Oke 1974; Fukugita et al. 1995). We use the standard Λ -dominated CDM cosmology with $\Omega_M = 0.3$, $\Omega_\Lambda = 0.7$, and $H_0 = 100h = 70 \text{ km s}^{-1} \text{ Mpc}^{-1}$, unless otherwise noted.

2. Our sample of extended Ly α sources

The targets of our current work were selected from the photometric sample constructed in Paper1, based on an intermediate-band imaging survey (Subaru proposal ID S02B-163: Kodaira et al.) with Subaru Prime-focus Camera (Suprime-Cam) mounted on 8.2m Subaru Telescope. The field of this survey is a blank field called Subaru/*XMM-Newton* Deep Field South (SXDF-S) located at $\alpha = 02^h 18^m 00^s$, $\delta = -05^\circ 25' 00''$ (J2000). The selection of extended Ly α sources was based on photometry in seven intermediate (IA) bands centered at $\sim 5000 - 7100 \text{ \AA}$ (Hayashino et al. 2000),

the B band, and a broadband redward of the $\text{Ly}\alpha$ line (R , i' , or z' band). The broadband data were taken in a large project of Subaru Telescope, Subaru/*XMM-Newton* Deep Survey (SXDS: Sekiguchi et al. 2004). The details of the selection are reported in Paper1. This sample consists of 41 objects, all of which are basically $\text{Ly}\alpha$ emitters with B -dropout, located at redshifts of $3.24 \lesssim z \lesssim 4.95$. Their photometric properties are listed in Table 3 of Paper1.

Their $\text{Ly}\alpha$ line luminosities measured with the IA-band photometry are typically $\sim 10^{42} - 10^{43} \text{ ergs s}^{-1}$. They are spatially extended in $\text{Ly}\alpha$ line, and faint and/or compact in the continuum redward of the $\text{Ly}\alpha$. They can be divided into two minor classes; “continuum-compact” objects and “continuum-faint” objects. About a half of them, 22 objects, can be regarded as point-sources in the redward continuum, and are classified as continuum-compact objects. They show B band dropout, which is consistent with Lyman break feature of distant galaxies at $z \gtrsim 3$. The remaining 19 objects are continuum-faint objects, which are fainter than 3σ in the redward continuum band. Their continuum break between the redward band and the B band cannot be measured since they are not detected in the B band. Some of these continuum-faint objects appear to be larger than the PSF size in the redward continuum band, but the sizes measured here are not reliable due to the low signal-to-noise (S/N) ratio.

Since our IA bands have relatively low sensitivities to the line emission compared with usual narrowbands, we can select objects with large equivalent widths (EWs). Our selection criteria correspond to the EWs greater than $\sim 55\text{\AA}$ in the rest frame. We roughly estimated the EWs with the photometric data, and found that the largest value is $\sim 700\text{\AA}$. The $\text{Ly}\alpha$ line luminosities are also relatively large, ranging from several $\times 10^{42} \text{ ergs s}^{-1}$ to $\sim 1 \times 10^{43} \text{ ergs s}^{-1}$. This corresponds to the luminous-end of the luminosity function (LF) of normal LAEs at similar redshifts. Figure 1 shows a comparison of the LF between our sample and a sample of LAEs at $z \simeq 3.7$ from a narrowband survey of SXDF (Ouchi et al. in preparation). The completeness of Ouchi et al.’s is $\sim 70 - 80\%$ at $\leq 24.2 \text{ mag}$ ($\gtrsim 3.4 \times 10^{42} \text{ ergs s}^{-1}$) and $\sim 50\%$ at $\leq 24.7 \text{ mag}$ ($\gtrsim 5.4 \times 10^{42} \text{ ergs s}^{-1}$). This comparison may suggest that a significant fraction ($\sim 10 - 20\%$) of luminous LAEs are spatially extended $\text{Ly}\alpha$ sources. However, one object in our sample at $z \simeq 3.7$, IB10-90651, is not included in this LAE sample down to 24.7 mag. This is due to the low surface brightness of this object and the relatively shallow exposure of the narrowband image.

Figure 2 shows the redshift distribution of our objects, based on the IA imaging (two double-counted objects are not eliminated). The detection limit of each IA band is also plotted in this figure. This shows that extended $\text{Ly}\alpha$ sources commonly exist in the early universe, almost independently of redshift. The size distribution of our objects is shown in Figure 3. There is no significant redshift dependence in the spatial extent. Note that the low sensitivity to the line emission also affects the apparent spatial extents of our objects, especially in higher redshift bands. The diffuse emission at the outskirts becomes more difficult to be detected, and the apparent sizes tend to become smaller. This is also suggested from Figure 2, in which the number of objects declines with redshift. True sizes may be larger than our estimation, and the size distribution may resemble that of M04’s LAB sample. Detailed simulations of such effects are presented in Paper1.

From the sample of 41 photometrically-selected objects, we selected 21 objects for further follow-up spectroscopy described below. About a half of them (11 objects) are continuum-compact objects, and another half (10 objects) are continuum-faint objects. As noted below, we could not obtain the spectra of three objects: IB11-101786 (continuum-faint), IB13-62009 (continuum-faint), and IB14-62116 (continuum-compact). Excluding these three, we obtained a spectroscopic sample of 18 objects (10 continuum-compact, and 8 continuum-faint objects). Photometric properties of the 18 objects are briefly summarized in Table 1, and their images are shown in Figure 4. Seven of them were spectroscopically confirmed to be high- z Ly α emitters (Paper1).

3. VIMOS spectroscopy

3.1. Observations

We used Visible Multi Object Spectrograph (VIMOS) mounted on the 8.2m Very Large Telescope (VLT) UT3 “Melipal” to take deep spectra for the objects selected above, under the program ID 074.A-0524. The observations were made during three dark nights of the visitor mode run on 2004 November 6 to 9 (UT). Two masks were used in multi-object spectroscopy (MOS) mode of VIMOS, covering the 21 objects. Two of them, IB11-101786 and IB13-62009, were too faint to be detected with the current depth of our spectroscopy. For another one object, IB14-62116, the Ly α line was almost completely overlapped with a strong sky emission line that cannot be correctly subtracted. We thus obtained spectra for 18 objects. In this run, the HR-Orange grism and the GG435 order-cut filter were used. This setting gives a spectral resolution $R = \Delta\lambda/\lambda \approx 2160$ ($\Delta\lambda \approx 2.8\text{\AA}$ at $\lambda = 6000\text{\AA}$) with a $1''.0$ wide slit. This spectral resolution corresponds to a velocity resolution of $\approx 140 \text{ km s}^{-1}$.

VIMOS has a wide FoV consisting of four quadrants of $\sim 7' \times 8'$ each, which can cover about 1/3 of a single Suprime-Cam FoV. The sky distribution of our objects and the VIMOS FoV are shown in Figure 5. The two MOS masks cover ten and eight objects, respectively. The integration time was 9.5 hrs and 8.0 hrs, respectively. During this run, the shutter unit for the second (north-eastern) quadrant often did not work correctly, and several exposures (30 minutes each) were lost. As a consequence, the integration time for each quadrant ranges from 6.5 hrs to 9.5 hrs. The seeing size varied during the three nights from $\lesssim 0''.5$ to $\sim 2''.4$. We flagged the frames with seeing worse than $\sim 1''.0$, so that the effective integration times of objects range from 4.0 hrs to 7.0 hrs. e standard star frames were taken at the end of the run. We used LTT3864, an F-dwarf located at $\alpha = 10^h 32^m 13.90^s$, $\delta = -35^\circ 37' 42''.4$ (J2000) as a standard star.

3.2. Primary reduction and flux measurement

The primary reduction was made with the VIMOS pipeline recipes 1.0 provided by ESO. This software package performs flat-fielding, distortion correction, wavelength calibration, and sky subtraction. The spectral resolution was measured to be $R \approx 2200$, using the sky emission lines. This resolution is sufficient to resolve the Ly α line profiles of our objects, which are known to have velocity widths less than several 100 km s^{-1} (§4.2 of Paper1). After primary reduction using the VIMOS pipeline, we performed flux calibration and further analysis using our original software. For the two-dimensional spectra, we smoothed the data with Gaussian kernel with FWHM of 4×5 pixels, which corresponds, to 3.22 \AA (wavelength axis) $\times 1''.0$ (spatial axis). To measure the fluxes and the velocity width on the one-dimensional spectra, we used 5-pixel smoothing, roughly corresponding to the current spectral resolution. We then measured the central wavelengths, fluxes, and velocity widths of the Ly α lines. The spectra thus obtained are shown in Figure 6.

3.3. Luminosity and velocity width of the Ly α line

The Ly α fluxes were calculated by correcting for the fraction of their line fluxes collectable with the $1''.0$ wide slitlets (slit-loss correction). The slit-loss correction was made by the following procedure by combination of photometric and spectroscopic data. We first assumed that (1) the intrinsic continuum spectra are flat within the bandpass of the IA filters, and that (2) the continuum levels are equal to that measured with the broadband redward of the Ly α line. Then we calculated the effect of the IGM absorption to the continuum using the redshift information obtained with the spectroscopy by following the formulation of Madau (1995). The pure Ly α line fluxes can be estimated by subtracting the continuum contribution from the IA photometry. We made this estimation of the total flux within an automatic aperture, F_{total} , and the flux within the slit we used, F_{slit} . The fraction of the collectable flux was then estimated by taking the ratio of the flux values measured with the both apertures, i.e., the slit-loss correction was applied by multiplying the line fluxes (from spectra) with $\frac{F_{total}}{F_{slit}}$.

The Ly α line fluxes thus obtained, $F(\text{Ly}\alpha)$, are shown in Table 2, together with the values before the slit-loss correction. The errors listed in Table 2 are estimated by integrating the 1σ noise level of the spectra over the range we integrated the flux of the Ly α line.

The Ly α line luminosities were directly calculated from these flux values by using the redshifts obtained spectroscopically. We fitted a Gaussian function to the line profile of each object, and defined the line center as the central wavelength of the Gaussian. Then we determined the redshift from the wavelength of the line center, and calculated the luminosity, $L(\text{Ly}\alpha)$, from the flux and the luminosity distance at the redshift. The velocity widths (FWHM) were measured simultaneously by using the redshifts obtained by the Gaussian fitting. We defined the zero velocity as the line center described above, and calculated the line-of-sight velocities of the wavelengths at which the flux density becomes a half of the peak value. The upper and lower limits of the FWHM were

estimated by measuring the full velocity widths at (half maximum) $\pm 1\sigma$.

3.4. Equivalent widths of the Ly α line

Since most of our objects do not show any continuum emission, we cannot obtain their EWs solely from the spectral data. Instead, we used the photometric data (broadband redward of the Ly α line) to estimate the continuum flux densities. The continuum flux densities were estimated using a $2''\phi$ aperture. Since we measure the EWs using the total flux of the Ly α line, this may cause an underestimate of the UV flux densities. For continuum-compact objects, this does not affect the results since the spatial extent is small enough. For continuum-faint objects, the spatial extents are generally larger than the PSF size (see Fig.2 of Paper1). However, they are fairly faint in continuum ($< 3\sigma$) and the measurement of their size is not so reliable. This implies that using a larger aperture make the measurement more sensitive to the sky fluctuation.

Then we divided the Ly α line fluxes obtained spectroscopically (slit-loss corrected) with the continuum fluxes obtained photometrically. Their rest-frame EWs, EW_{rest} , are also shown in Table 2. All the objects in our sample have fairly large EWs with a median value of $EW_{\text{rest}} \approx 210\text{\AA}$. For 9 out of 18 objects, the EW_{rest} exceed 200\AA . Eight out of these nine objects are continuum-faint objects, having yet larger EWs exceeding 240\AA , i.e., all of the continuum-faint objects in our VIMOS sample have large EWs. Another object with $EW_{\text{rest}} > 200\text{\AA}$, IB12-58572, is a continuum-compact object, but its continuum level is the lowest among all the continuum-compact objects in our VIMOS sample ($\sim 3.5\sigma$). We plot the EWs as a function of the Ly α line luminosity in Figure 7. The nine objects with $EW_{\text{rest}} > 200\text{\AA}$ apparently show a positive correlation between the luminosity and the EW. This is thought to be an artifact caused by the detection limits in the redward continuum bands. For these nine objects (or at least eight continuum-faint objects), the EWs we measured are likely to be still larger, since the continuum levels are close to the sky fluctuation level. For the remaining nine objects, our measurement of the EWs is somewhat more accurate than for objects with large EWs, since the continuum levels exceed 3.7σ .

The upper and lower limits for the EWs are estimated as follows. Since the denominators in the calculation of EWs are very small values, and the errors in EWs are dominated by the photometric errors in the broadband images. We estimated the error using the limiting magnitudes of the broadband images used to estimate the continuum levels: 27.4 mag for R and 27.0 for i' (3σ , $2''\phi$ aperture). The upper and lower limits of the EWs, EW_{upper} and EW_{lower} , were estimated from

$$EW_{\text{upper}} = (F(\text{Ly}\alpha) + \text{err}[F(\text{Ly}\alpha)]) / (f_{\lambda} - \text{err}[f_{\lambda}]),$$

and

$$EW_{\text{lower}} = (F(\text{Ly}\alpha) - \text{err}[F(\text{Ly}\alpha)]) / (f_{\lambda} + \text{err}[f_{\lambda}]),$$

where $F(\text{Ly}\alpha)$ is the Ly α line flux, f_{λ} is the continuum flux density, and $\text{err}[\]$ denotes the 1σ noise level.

Note that our measurements of EWs are likely to underestimate the intrinsic value, since we did not make any correction for the IGM absorption of the Ly α emission.

3.5. Wing component analysis

Although most of our objects have relatively small velocity widths, some objects have broad wing emission of the Ly α line. The Ly α line profile of IB10-90651, for example, has broad wing emission on the red side, while the blue side shows a relatively sharp cut-off. Such features of the line profile must reflect the kinematics of Ly α emitting gas, and should act as a diagnostic of inflow / outflow activities in the system. In order to identify such high velocity wing components in the Ly α line profiles, we performed a quantitative analysis for all the objects in our spectroscopic sample. To identify such faint wing components, we need to have spectra of sufficiently high S/N ratios. We therefore used 8-pixel smoothing after integrating the spectra along the slit direction. Although the 8-pixel smoothing reduces the spectral resolution to $\sim 5\text{\AA}$, this resolution is still high enough to investigate the gas dynamics with the line profile.

The procedure of the analysis is similar to that described in §3.3, except the smoothing width of 8-pixel. After obtaining improved S/N ratios by smoothing the one-dimensional spectra, we fitted a simple Gaussian function to the Ly α line profile of each object. We then plotted the excess of the spectrum from the Gaussian function against the line-of-sight velocity. If the excess of the spectrum greater than 2σ has a velocity width greater than 250 km s^{-1} (corresponds to 8-pixels), we here refer to it as the “excess”. If the excess appears from within the 2σ -width of the Gaussian peak and continuous beyond $\pm 500\text{ km s}^{-1}$ from the line center, we define it as “wing emission”. The plots thus obtained are shown in Figure 6, and the results are also summarized in Table 2. For at least five objects, IB10-17108, IB10-32162, IB10-54185, IB10-90651, and IB14-52102, we identified high velocity wing emission on the red side of the Ly α line. On the other hand, none of our objects shows significant wing emission on the blue side. Just two objects, IB12-30834 and IB12-58572, *marginally* show a blue wing.

4. Results and discussion

Summarizing the results obtained in the previous section, we categorize our objects according to the spectral properties. We can classify our objects in two ways, i.e., in terms of EWs and wing emission in the line profile. In terms of EWs, we divide our VIMOS sample into two EW classes. The moderate EW class has $100\text{\AA} < \text{EW} < 200\text{\AA}$ while the large EW class has $\text{EW} > 200\text{\AA}$ (see Figure 7). The value of $\text{EW} = 200\text{\AA}$ is fairly large for ordinary starbursts. The large EW class and the small EW class roughly correspond to continuum-compact objects and continuum-faint objects, respectively. In terms of the line profile, we can also classify our objects into two groups, i.e., those with broad asymmetric wing on the red side, and those with no clear signature of such

wing emission.

4.1. Objects with moderate EWs

The nine objects in the smaller EW group, IB08-86220, IB10-17108, IB10-32162, IB10-54185, IB12-21989, IB12-71781, IB13-96047, IB14-47257, and IB14-52102, have EWs ranging between 100Å and 200Å. This EW range is the regime of stellar photo-ionization with a solar metallicity, an upper mass cut-off of $100M_{\odot}$, and an IMF slope up to 1.5 (Charlot & Fall 1993). The EWs of these objects thus can be explained in terms of photo-ionization by moderately old stellar populations, not necessarily requiring an extremely top-heavy IMF or a zero-metallicity. The most conservative explanation for these objects are thus ordinary starbursts. The large spatial extent of Ly α emission can be understood as a result of resonant-scattering of Ly α photons (e.g. Møller & Warren 1998; Laursen & Sommer-Larsen 2006).

Assuming that the ionizing sources for these objects are ordinary starburst. we can give rough estimates of the star formation rates (SFRs) of these objects. We here assume Salpeter’s IMF, stellar mass range of $0.1 - 100M_{\odot}$, solar metallicity, no extinction, and the case B recombination in the low-density limit ($N_e \ll 1.5 \times 10^4 \text{cm}^{-3}$). We can then use a conversion law of $L(\text{Ly}\alpha) = 1 \times 10^{42} (\text{SFR}/M_{\odot}\text{yr}^{-1} \text{ergs s}^{-1})$ to estimate their SFRs (Osterbrock 1989; Kennicutt 1998). Their SFRs thus estimated are $3.3 - 13 M_{\odot} \text{yr}^{-1}$, which are located within the range of normal LAEs known to date (e.g. Fynbo et al. 2003; Rhoads et al. 2003; Dawson et al. 2004).

However, their physical nature, even the SFR, is poorly constrained because of the large uncertainties in dust / IGM absorption, stellar mass function, and the contribution from non-stellar processes. Some of the objects indeed show asymmetric line profiles suggesting superwind activities (see §4.2 below). The possibility of the existence of AGNs, although unlikely, also cannot be eliminated completely. Notes for individual objects in this group are summarized in appendix A.1.

4.2. Objects with broad asymmetric wings

As described in §3.5, five objects, IB10-17108, IB10-32162, IB10-54185, IB10-90651, and IB14-52102, have asymmetric broad wing emission on the Ly α line profile. These objects have conspicuous high velocity wing components on the red side, and a relatively sharp cut-off on the blue side of the Ly α line. Their wing emission components are extended up to $\gtrsim 500 \text{km s}^{-1}$ from the line centers, and no clear counterparts are found on the blue side. The origin of such asymmetry, which is commonly seen in high- z Ly α emission, is thought to be either absorption by intervening neutral hydrogen (Lyman forest absorption), or galactic superwind. Although these two mechanisms cannot be definitely discriminated, the spectra of these five objects show some evidence that favor the existence of superwind activities as shown below.

No significant continuum emission is detected in any of the 18 objects in our sample. Only one object, IB12-21989, showed marginal signature of continuum emission with $\sim 2\sigma$ level of the sky fluctuation, but this object does not have the red wing. This implies that the contribution of the continuum to the wing components we identified is negligible, and there should be a high velocity Ly α emission component within the systems. An asymmetric line profile with a broad red wing and a sharp blue cut-off is commonly seen in superwind galaxies (e.g. Ajiki et al. 2002; Dawson et al. 2002), and well agrees with theoretical predictions of the superwind model (Tenorio-Tagle et al. 1999).

In fact, one of these five objects with red wings, IB10-90651, shows a systematic velocity structure on the two-dimensional spectrum (second part of Figure 6, top-left panel). This object has an extremely extended, diffuse emission component on the red side of the Ly α . It extends up to 5'' (projected distance of 36 kpc at $z = 3.68$) toward south from the center of the object, and the velocity extent is $\sim 1000 \text{ km s}^{-1}$ redward from the line center. On the blue side, although fairly faint, we can see a counter-image of the diffuse component extending toward north. These velocity structures suggest that this object has a galactic superwind flowing nearly along the position angle of the slit. The faintness of the blue component can be explained with absorption by the near-side shell of H I gas, while the flux of the red component is enhanced by back-scattering by the far-side shell (Tenorio-Tagle et al. 1999).

Although the blue counter-image can be seen in the two-dimensional spectrum of IB10-90651, we cannot see blue wing emission on the one-dimensional spectrum. This asymmetric profile is quite similar to other four objects. This suggests that all the five objects with red wings are likely to be superwinds. The fraction of such objects in our sample, $5/18 \simeq 30\%$, is similar to that of sub-mm detection in M04's sample (Geach et al. 2005). Such sub-mm detection suggests the existence of obscured starburst regions responsible for extended Ly α emission, i.e., superwinds. The lack of diffuse and extended high velocity components may suggest either that the direction of outflow is perpendicular to the slit direction, or that the Ly α emission is intrinsically faint. The former possibility should be examined by further deep spectroscopy with various slit direction or an integral field spectroscopy. The latter is quite consistent with the relatively small EWs of the four objects with red wings. When the contribution of superwind activities is relatively small, the EWs of the Ly α emission should be smaller than superwind-dominated sources like IB10-90651.

Note that there are some other objects that possibly have red side wings, e.g. IB12-81981 ($\sim 1.5\sigma$ up to $\sim 400 \text{ km s}^{-1}$). However, the wing components of such objects, if any, are fairly faint, and affected by neighboring sky emission lines for most cases. If they indeed have wing emission on the red side, they are also likely to have superwind activities within the systems. Other notes for each object are listed in appendix A.2

4.3. Objects with large EWs and no wings

After classifying our objects in two ways, there remains eight objects that have large EWs and no significant wing emission on the red side of the Ly α line: IB11-59167, IB11-80344, IB11-89537, IB12-30834, IB12-48320, IB12-58572, IB12-81981, and IB13-104299. Except for one, IB12-58572, they are all continuum-faint objects (see §2) with $EW_{\text{rest}} > 240\text{\AA}$. The EW of 240\AA is predicted for the starbursts with solar metallicity at an age of 10^6 yrs by Charlot & Fall (1993), and also predicted by MR02 by introducing an extremely top-heavy IMF (slope = 0.5) or zero-metallicity, for starbursts with an age of $\gtrsim 10^7$ yrs. As mentioned above in §3.4, the observed EWs should be smaller than intrinsic values due to the absorption of Ly α emission by the IGM. Namely, the seven continuum-faint objects have EWs securely exceeding 240\AA .

For these eight sources, the origin of the Ly α emission is hardly thought to be *ordinary* starbursts. If their ionizing sources are starbursts, the large EWs require photo-ionization by extremely young stellar populations (age $\ll 10^7$ yrs) with an extremely top-heavy IMF and/or very low metallicity. In this case, the stellar components should be dominated by population III stars. Calculations by MR02 show that a stellar population with zero-metallicity and Salpeter’s IMF can achieve an extremely large EW, 1122\AA at the age of 10^6 yrs. Schaerer (2003) also suggests by treating various IMFs and stellar mass ranges that, under very metal-poor conditions, the EWs of Ly α emission from very young starbursts can be highly enhanced, $\sim 1300\text{\AA}$ at an age of 10^6 yrs. In this picture, the extended Ly α emission can be attributed to resonant-scattering. In addition, it is thought that cooling radiation or supernova explosions also contribute to the Ly α emission, at least in some part.

As for the starbursts, it is also possible that the starburst regions are heavily obscured by dust with somewhat an inhomogeneous distribution. If the dust screen absorbs UV photons traveling along the line of sight, the observed faintness in UV continuum can be reproduced. Then if UV photons traveling along other directions are not significantly absorbed, they can ionize the H I gas surrounding the starburst region, and can lead to spatially extended Ly α emission. Since UV continuum emission cannot be scattered in this manner, these processes can at least qualitatively explain the extended Ly α emission and faint / compact UV continuum emission. This is thought to be a plausible explanation because galaxies in high redshifts are generally surrounded by a larger amount of H I gas than galaxies in the present universe (e.g. Adelberger et al. 2003). The Ly α emitting gas will be spatially more extended than the starburst region, and thus less sensitive to dust absorption.

If the dust screen covers the whole direction, even Ly α photons cannot escape the system. Instead, the star forming activities can lead to shock-ionization by a superwind (e.g. Taniguchi & Shioya 2000; Taniguchi et al. 2001; Veilleux et al. 2005). However, we could not detect significant high-velocity components on the Ly α line profiles, nor on the two-dimensional spectra. If superwind activities are responsible for the extended Ly α emission for these objects, the shocked region associated with the wind, if any, should be very faint. Their relatively small velocity widths of the Ly α line, typically $\sim 300 - 500 \text{ km s}^{-1}$, also suggests that powerful superwinds are unlikely. The

exception is two objects, IB11-80344 and IB11-89537, which have relatively large velocity widths up to $\sim 740 \text{ km s}^{-1}$. These objects might be superwinds, but have smaller velocity widths than the most prominent ones known to date (e.g. $\sim 10^3 \text{ km s}^{-1}$, Heckman et al. 1990). Additionally, note that there are some objects that have a *marginal* signature of wing emission on the red side of the Ly α , e.g. IB12-48320 and IB12-81981. The red side spectra of these objects are overlapped with relatively strong sky emission lines which cannot be subtracted completely. If a deeper exposure and/or a more sufficient sky subtraction become available, we can possibly detect a high velocity wing component on the line profile for some objects.

Apart from such uncertainties, the eight objects show a remarkable feature. Figure 8 plots the velocity width as a function of the Ly α line luminosity. If the ionizing mechanism is cold accretion, the velocity width will roughly correspond to the circular velocity of the system, and thus will be scaled to the mass of the system. On the other hand, the Ly α luminosity should be positively correlated with the gravitational energy of the system, and thus scaled to the mass of the system. Therefore, the velocity width and the Ly α line luminosity should have a positive correlation. Among all the objects in our VIMOS sample, the eight objects with large EWs and no wings clearly show a positive correlation in Figure 8. Although not a definite constraint, this result supports the idea of cooling radiation. Their relatively small velocity widths quite well agree with a theoretical prediction of cooling radiation (Fardal et al. 2001). Even for the two objects with large velocity widths ($\Delta V > 500 \text{ km s}^{-1}$), these velocity widths can be reproduced by taking into account the effect of resonant-scattering, or perhaps an additional ionizing source in the system (Dijkstra et al. 2006a,b). Furthermore, two or more objects (e.g. IB12-58572 and IB12-104299) marginally show an odd asymmetry of the line profile, i.e., broader on the blue side than on the red side, which also agrees with the prediction of Dijkstra et al. (2006a). Thus, cooling radiation can be a reasonable explanation for these eight objects. It is also true that other mechanisms contribute to the Ly α emission, together with cold accretion. Such additional mechanisms are discussed in §4.4 Notes for individual objects are described in appendix A.3.

4.4. Constraints from other data

We have mentioned about four possibilities for the origins of the spatially extended Ly α emission: stellar photo-ionization, photo-ionization by AGNs, shock-heating by superwinds, and cooling radiation from infalling material (cold accretion). These scenarios predict characteristic emission lines of each ionizing source. In addition to our VIMOS data, we can use the data taken in our previous study and X-ray data for diagnostics of the physical origins. We then first analyzed the low-resolution spectroscopic data taken with FOCAS on Subaru Telescope, and the IA images taken with Suprime-Cam (Paper1) to detect the emission lines.

For starbursts, there are two cases described in §4.3, i.e., extremely young starbursts dominated by population III stars, and starbursts heavily obscured by dust. The former case of starbursts has an extremely low metallicity and a top-heavy IMF. Such an extremely young stellar population

formed in a primordial condition should have He II $\lambda 1640$ emission (Schaerer 2003). The He II line is also predicted for the case of cooling radiation (Yang et al. 2006). While Ly α line is optically thick in general, this line should be optically thin. This implies that the He II line is suitable to probe the gas dynamics, and thus a good probe to discriminate stellar photo-ionization and cooling radiation. However, none of our objects in the FOCAS spectroscopic sample has detectable He II emission. On the composite spectrum, there is apparently an emission feature at the wavelength of rest-frame 1640Å (see Figure 4 of Paper1). This is just a marginal signature since the wavelengths near the rest-frame 1640Å is largely affected by sky emission lines.

For the case of obscured starbursts, there should be characteristic metal lines, such as [O II] $\lambda 3727$, [O III] $\lambda\lambda 4959, 5007$, and H α $\lambda 6563$. These lines are less sensitive to dust absorption than the Ly α line, and should be good diagnostics of starbursts, although they are redshifted beyond the wavelength coverage of our FOCAS data. Such metal lines can also be seen in superwind galaxies. The primordial gas surrounding galaxies should be chemically enriched by supernova explosions, resulting in spatially extended metal lines. Namely, superwind galaxies are expected to have spatially extended C IV line emission with a strength of $\sim 1/10$ of the Ly α line (Heckman et al. 1991b). We previously showed in Paper1 that there are no such metal emission lines either in the individual spectra or in the stacked spectrum, down to our current detection limits. This suggests that at least the majority of the FOCAS sample (seven objects) are unlikely to be superwinds. These pieces of evidence from the observations are, however, just weak constraints on the superwind scenario. In fact, IB10-90651 is proved to have extended diffuse emission components by performing deep spectroscopy. Further deep follow-up observations may find diffuse emission components suggesting the superwind scenario.

The C IV emission line, as well as N V or He II lines, can also be diagnostics of the AGN activities. Similarly to superwinds, AGN scenario is also likely to be ruled out by the absence of the C IV or N V lines on the FOCAS spectra. Our IA images show that, although they are more extended than point-sources, the sizes of Ly α emission components are typically $\sim 10 - 15$ kpc, and are smaller than those of Ly α nebulae associated with AGNs (e.g. Heckman et al. 1991a; Weidinger et al. 2004, 2005). The velocity widths of our objects are also smaller than those of Ly α nebulae associated with AGNs known to date (e.g. van Ojik et al. 1997; Weidinger et al. 2004, 2005). Together with the faintness in UV continuum, these facts suggest that if the ionizing sources are AGNs, they must be obscured (type II) AGNs. In order to examine such AGN activities, it is important to compare them with type II QSOs known to date. Type II AGNs are, however, suggested to be quite rare by photometric studies of LAE samples (Malhotra et al. 2003; Wang et al. 2004). We will then just show the results of our analysis of X-ray data taken with *XMM-Newton*.

Most of our field is covered by X-ray data with two pointings of *XMM-Newton* (Ueda et al. 2007), and the X-ray flux limits can be estimated by using these data. The sensitivity is sufficient to detect bright quasars at $z \sim 4$. In order to put the strongest constraints, we here used the data of 0.5–4.5 keV band, the most sensitive band of *XMM-Newton*. We estimated the 1σ flux limits in the rest-frame 2–10 keV from the count rate limits, by assuming X-ray spectra of $F_e \propto \epsilon^{-0.8}$

and absorption with a hydrogen column density of $N_{\text{H}} = 1 \times 10^{23} \text{cm}^{-2}$ and $N_{\text{H}} = 1 \times 10^{24} \text{cm}^{-2}$. The flux limits thus estimated are listed in Table 3. The typical values of their flux limits in the case of $N_{\text{H}} = 1 \times 10^{23} \text{cm}^{-2}$ are a few $\times 10^{-15} \text{ergs cm}^{-2} \text{s}^{-1}$, which leads to X-ray luminosities $\sim 10^{45} \text{ergs s}^{-1}$ at $z \sim 4$. These are comparable to the X-ray luminosities of type II QSOs known to date (Norman et al. 2002; Stern et al. 2002; Dawson et al. 2003). Our analysis ignores the reflection components of X-ray emission, so that the upper limits listed in Table 3 are thought to be the most conservative values, i.e., the X-ray luminosities are likely to be significantly smaller than those of type II QSOs. Note that we cannot put any constraints if our objects are compton-thick, $N_{\text{H}} \gg 10^{24} \text{cm}^{-2}$. These imply that our objects are unlikely to be harboring type II QSOs, although the possibility of AGNs is not completely ruled out due to the relatively shallow exposure of the X-ray data.

5. Conclusions

We have carried out deep, medium-resolution ($R \sim 2000$) follow-up spectroscopy of 18 extended Ly α sources at $z \sim 3 - 5$ that are faint and/or compact in UV continuum, using VLT/VIMOS. We found that all 18 objects in our VIMOS sample have fairly large equivalent widths (EWs) of the Ly α emission with a median value of $\approx 210 \text{\AA}$ in the rest-frame. A half of our sample (nine objects) have moderately large EWs of $\sim 100 - 200 \text{\AA}$, and are accounted for by ordinary starbursts with a solar metallicity. The high resolution and S/N ratio of our data enabled us to make a quantitative analysis of the Ly α line profiles. The velocity widths were found to be relatively small, typically $\sim 300 - 500 \text{ km s}^{-1}$.

For five objects ($\sim 30\%$), we identified conspicuous broad wing emission components on the red side of the Ly α line, while no significant wing emission was found on the blue side. Such features quite well agree with theoretical predictions of galactic superwind model. Namely, we found diffuse high velocity emission components extended up to $\sim 70 \text{ kpc}$ on the two-dimensional spectrum of one of these five objects. The velocity extent of these components is $\gtrsim 2000 \text{ km s}^{-1}$ with systematic velocity structure, i.e., the southern part is redshifted and the northern part is blueshifted. These features suggest the existence of galactic superwind activities.

Excluding the objects above, there remain eight objects, which have large EWs exceeding 200\AA (seven have EWs exceeding 240\AA), and no clear signature of high velocity wing emission on the either side of the Ly α line. These objects are hardly thought to be ordinary starbursts, and our IA images and FOCAS spectra show no clear signature of AGN activities. Non-detection in X-ray data taken with *XMM-Newton* also suggests they are unlikely to be AGN-origin like type II QSOs. Their relatively small spatial extents and velocity widths agree well with theoretical predictions of cooling radiation. Furthermore, their velocity widths clearly show a positive correlation with the Ly α line luminosities. These facts suggest that they are candidates for forming-galaxies in gas-cooling phase, i.e., the very first stage of galaxy formation.

REFERENCES

- Adelberger, K. L., Steidel, C. C., Shapley, A. E., & Pettini, M. 2003, *ApJ*, 584, 45
- Ajiki, M., et al. 2002, *ApJ*, 576, L28
- Basu-Zych, A., Scharf, C. 2004, *ApJ*, 615, L85
- Birnboim, Y., & Dekel, A. 2003, *MNRAS*, 345, 349
- Bower, R. G., et al. 2004, *MNRAS*, 351, 63
- Chapman, S. C., Scott, D., Windhorst, R. A., Frayer, D. T., Borys, C., Lewis, G. F., & Ivison, R. J. 2004, *ApJ*, 606, 85
- Chapman, S. C., Lewis, G. F., Scott, D., Richards, E., Borys, C., Steidel C. C., Adelberger K. L., & Shapley A. E. 2001, *ApJ*, 548, L17
- Charlot, S., & Fall, S. M. 1993, *ApJ*, 415, 580
- Cowie, L. I., & Hu, E. M. 1998, *AJ*, 115, 1319
- Dawson, S., et al. 2004, *ApJ*, 617, 707
- Dawson, S., McCrady, N., Stern, D., Eckart, M. E., Spinrad, H., Liu, M. C., & Graham, J. R. 2003, *AJ*, 125, 1236
- Dawson, S., Spinrad, H, Stern, D., van Breugel, W., de Vries, W., & Reuland, M. 2002, *ApJ*, 570, 92
- Dekel, A., & Birnboim, Y. 2006, *MNRAS*, 368, 2
- Dey, A., et al. 2005, *ApJ*, 629, 654
- Dijkstra, M., Haiman, Z., Spaans, M. 2006a, *ApJ*, 649, 14
- Dijkstra, M., Haiman, Z., Spaans, M. 2006b, *ApJ*, 649, 37
- Fardal M., Katz N., Gardner J. P., Hernquist, L., Weinberg, D. H., Romeel, D. 2001, *ApJ*, 562, 605
- Francis, P. J., et al. 2001, *ApJ*, 554, 1001
- Fukugita, M., Shimasaku, K., & Ichikawa, T. 1995, *PASP*, 107, 945
- Furlanetto, S., Schaye, J., Springel, V., & Hernquist, L. 2004, *ApJ*, 622, 7
- Fynbo, J. U., Møller, P., & Thomsen, B. 2001, *A&A*, 374, 443
- Fynbo, J. P. U., Ledoux, C., Møller, P., Thomsen, B., & Burud, I. 2003, *A&A*, 407, 147

- Geach, J. F. et al. 2005, MNRAS, 363, 1398
- Haiman, Z., Spaans, M., & Quataert, E. 2000, ApJ, 537, L5
- Haiman, Z., & Rees, M. J. 2001, ApJ, 556, 87
- Hayashino, T., et al. 2000, Proc. SPIE, 4008, 397
- Heckman, T. M., Armus, L., Miley, G. K. 1990, ApJS, 74, 833
- Heckman, T. M., Lehnert, M. D., van Breugel, W., & Miley, G. K. 199a, ApJ, 370, 78
- Heckman T. M., Lehnert M. D., Miley G. K., & van Breugel W. 1991b, ApJ, 381, 373
- Hu, E. M., Cowie, L. L., & McMahon, R. O. 1998, ApJ, 502, L99
- Iye, M., et al. 2006, Nature, 443, 1861
- Kashikawa, N., et al. 2005, PASJ, 648, 7
- Keel, W. C., Cohen, S. H., Windhorst, R. A., & Waddington I. 1999, AJ, 118, 2547
- Kennicutt, R. C., Jr. 1998, ARA&A, 36, 189
- Kodaira, K., et al. 2003, PASJ, 55, L17
- Laursen, P., & Sommer-Larsen, J. 2006, preprint (astro-ph/0610761)
- Madau P. 1995, ApJ, 441, 18
- Maier, C., et al. 2003, A&A, 402, 79
- Malhotra, S., Wang, J. X., Rhoads, J. E., Heckman, T. M., & Norman, C. A. 2003, ApJ, 585, L25
- Malhotra, S., & Rhoads, J. E. 2002, ApJ, 565, L71 (MR02)
- Matsuda, Y., Yamada, T., Hayashino, T., Yamauchi, R., & Nakamura, Y. 2006, ApJ, 640, L123
- Matsuda, Y., et al. 2004, AJ, 128, 569 (M04)
- McCarthy, P. J., van Breugel, W., Kapahi, V. K., & Subrahmanya, C. R. 1999, ApJ, 192, 522
- Mo, H. J., & White, S. D. M. 2002, MNRAS, 336, 112
- Møller, P., Warren, S. J. 1998, MNRAS, 299, 661
- Nilsson, K., Fynbo, J. P. U., Sommer-Larsen, J., & Ledoux, C. 2006, 452, L23
- Norman, C., et al. 2002, ApJ, 571, 218
- Ohyama, Y., et al. 2003, ApJ, 591, L9

- Oke, J. B. 1974, *ApJS*, 27, 21
- Osterbrock, D. E. 1989, “*Astrophysics of Gaseous Nebulae and Active Galactic Nuclei*”, University Science Books
- Ouchi, M., et al. 2005, *ApJ*, 620, L1
- Ouchi, M., et al. 2003, *ApJ*, 582, 60
- Palunas, P., Teplitz, H. I., Francis, P. J., Williger, G. M., & Woodgate, B. E. 2004, *ApJ*, 602, 545
- Partridge, R. B., & Peebles, P. J. E. 1957, *ApJ*, 148, 377
- Rhoads, J. E., et al. 2003, *AJ*, 125, 1006
- Rhoads, J. E., Malhotra, S., Dey, A., Stern, D., Spinrad, H., & Jannuzi, B. T. 2000, *ApJ*, 545, L85
- Saito, T., Shimasaku, K., Okamura, S., Ouchi, M., Akiyama, M., & Yoshida, M. 2006, *ApJ*, 648, 54
- Schaerer, D. 2003, *A&A*, 397, 527
- Sekiguchi K., et al. 2004, *Ap&SS*, 301, 169
- Shimasaku, K., et al. 2003, *ApJ*, 586, L111
- Steidel, C., Adelberger, K. T., Shapey, A. E., Pettini, M., Dickinson, M., & Giavalisco, M. 2000, *ApJ*, 532, 170 (S00)
- Stern, D., et al. 2002, *ApJ*, 568, 71
- Taniguchi, Y., & Shioya, Y. 2000, *ApJ*, 532, L13
- Taniguchi, Y., Shioya, Y., & Kakazu, Y. 2001, *ApJ*, 562, L15
- Tenorio-Tagle, G., Silich, S. A., Kunth, D., Terlevich, E., & Terlevich, R. 1999, *MNRAS*, 309, 332
- van Ojik R., Röttgering H. J. A., Miley G. K., & Hunstead R. W. 1997, *A&A*, 317, 358
- Veilleux, S., Cecil, G., & Bland-Hawthorn, J. 2005, *ARA&A*, 43, 769
- Wang, J. X., et al. 2004, *ApJ*, 608, L21
- Weidinger, M., Møller, P., & Fynbo, J. P. U. 2004, *Nature*, 430, 999
- Weidinger, M., Møller, P., Fynbo, J. P. U., & Thomsen, B. 2005, *A&A*, 436, 825
- Wilman R. J., Gerssen J, Bower R. G., Morris S. L., Bacon R., de Zeeuw P. T., & Davies R. L. 2005, *Nature*, 436, 227

Yang, Y., Zabludoff, A. I., Davé, R., Eisenstein, D. J., Pinto, P. A., Katz, N., Winberg, D. H., & Barton, E. J. 2006, ApJ, 640, 539

A. Notes for individual objects

A.1. Objects with moderate EWs

IB08-86220 $z = 3.31$, $\text{SFR} \simeq 3.3 M_{\odot} \text{yr}^{-1}$, $\text{EW}_{\text{rest}} \simeq 120 \text{\AA}$. Even the upper limit of EW does not exceed 200\AA . Our analysis may suffer from relatively large residuals of the sky emission at $\approx 5225 \text{\AA}$ and $\approx 5240 \text{\AA}$.

IB10-17108 $z = 3.79$, $\text{SFR} \simeq 10 M_{\odot} \text{yr}^{-1}$, $\text{EW}_{\text{rest}} \simeq 110 \text{\AA}$. The EW is the smallest in our sample, and the uncertainty in the EW is relatively small. Wing emission can be seen on the red side (see appendix A.2).

IB10-32162 $z = 3.74$, $\text{SFR} \simeq 9.7 M_{\odot} \text{yr}^{-1}$, $\text{EW}_{\text{rest}} \simeq 150 \text{\AA}$. The upper limit of the EW is relatively large for this group of objects, $\simeq 180 \text{\AA}$. The velocity width is relatively large, $\Delta V \simeq 610 \text{ km s}^{-1}$ (FWHM). Wing emission can be seen on the red side (see appendix A.2).

IB10-54185 $z = 3.82$, $\text{SFR} \simeq 6.5 M_{\odot} \text{yr}^{-1}$, $\text{EW}_{\text{rest}} \simeq 130 \text{\AA}$. The velocity width is quite small, $\Delta V \simeq 300 \text{ km s}^{-1}$. Wing emission can be seen on the red side (see appendix A.2).

IB12-21989 $z = 4.11$, $\text{SFR} \simeq 13 M_{\odot} \text{yr}^{-1}$, $\text{EW}_{\text{rest}} \simeq 180 \text{\AA}$. Continuum emission can be seen at $\simeq 1.5\sigma$ level, and the EW calculated directly from the spectrum is $\simeq 35 \text{\AA}$. Our photometry may suffer from neighboring continuum sources.

IB12-71781 $z = 4.11$, $\text{SFR} \simeq 4.1 M_{\odot} \text{yr}^{-1}$, $\text{EW}_{\text{rest}} \simeq 130 \text{\AA}$. The upper limit of the EW is fairly large, $\simeq 230 \text{\AA}$, so that this object is possibly not categorized as an ordinary starburst. Our analysis may suffer from the several sky emission lines on the red side of the Ly α (e.g. $\approx 6235 \text{\AA}$).

IB13-96047 $z = 4.27$, $\text{SFR} \simeq 10 M_{\odot} \text{yr}^{-1}$, $\text{EW}_{\text{rest}} \simeq 140 \text{\AA}$. Even the upper limit of the EW does not exceed 200\AA . Our spectral analysis may suffer from neighboring several sky emission lines on the both sides of the Ly α . Neighboring continuum sources may affect our photometric analysis.

IB14-47257 $z = 4.66$, $\text{SFR} \simeq 13 M_{\odot} \text{yr}^{-1}$, $\text{EW}_{\text{rest}} \simeq 180 \text{\AA}$. With an upper limit of the EW $\simeq 240 \text{\AA}$, this object not be an ordinary starburst. The spectrum suffers from relatively strong residuals of the sky emission at $\approx 6865, 6900$, and 6910\AA near the Ly α line. The Ly α line itself is overlapped with weak sky emissions.

IB14-52102 $z = 4.47$, $\text{SFR} \simeq 9.0 M_{\odot} \text{yr}^{-1}$, $\text{EW}_{\text{rest}} \simeq 150 \text{\AA}$. With an upper limit of the EW $\simeq 200 \text{\AA}$, this object may not be an ordinary starburst. The line profile has wing emission on the red side (see appendix A.2).

A.2. Objects with broad asymmetric wings

IB10-17108 $z = 4.11$, $\text{EW}_{\text{rest}} \approx 130 \text{\AA}$, $\Delta V \approx 490 \text{ km s}^{-1}$. Also listed in appendix A.1. The wing component is very clear, and extended up to $\gtrsim 700 \text{ km s}^{-1}$ from the line center.

IB10-32162 $z = 3.74$, $\text{EW}_{\text{rest}} \approx 150 \text{\AA}$, $\Delta V \approx 610 \text{ km s}^{-1}$. Also listed in appendix A.1. The velocity width of the main component is fairly large, $\approx 610 \text{ km s}^{-1}$. The wing component is not very clear, but the line profile shows a significant asymmetry.

IB10-54185 $z = 3.82$, $\text{EW}_{\text{rest}} \approx 130 \text{\AA}$, $\Delta V \approx 300 \text{ km s}^{-1}$. Also listed in appendix A.1. The spectrum may suffer from sky emission lines on the red side ($\approx 5890 \text{\AA}$ and a weak one at $\approx 5870 \text{\AA}$), but the red side wing exceeds the 3σ noise level at $\lesssim 450 \text{ km s}^{-1}$ from the line center. The wing component can be seen up to $\sim 600 - 1000 \text{ km s}^{-1}$.

IB10-90651 $z = 3.68$, $\text{EW}_{\text{rest}} \approx 860 \text{\AA}$, $\Delta V \approx 570$. The EW is the largest in our sample. The wing emission is extended up to $\gtrsim 500 \text{ km s}^{-1}$. A systematic velocity structure of diffuse emission can be seen in the two-dimensional spectrum.

IB14-52102 $z = 4.47$, $\text{EW}_{\text{rest}} \approx 150 \text{\AA}$, $\Delta V \approx 350 \text{ km s}^{-1}$. Also listed in appendix A.1. The wing component exceeds the 3σ noise level, and is extended up to $\sim 500 \text{ km s}^{-1}$.

A.3. Objects with large EWs and no wings

IB11-59167 $z = 3.94$, $\text{EW}_{\text{rest}} \approx 270 \text{\AA}$, $\Delta V \approx 270 \text{ km s}^{-1}$. A systematic (outflow-like) velocity structure may exist, but the spectrum may suffer from incomplete sky subtraction at $\approx 6000 \text{\AA}$.

IB11-80344 $z = 3.89$, $EW_{\text{rest}} \approx 569\text{\AA}$, $\Delta V \approx 740\text{ km s}^{-1}$. The lower limit of the EW is $\approx 380\text{\AA}$. The velocity width is large, and the line profile has a double-peaked shape. The spectrum may suffer from several sky emission lines.

IB11-89537 $z = 4.03$, $EW_{\text{rest}} \approx 460\text{\AA}$, $\Delta V \approx 560\text{ km s}^{-1}$. The lower limit of the EW is $\approx 300\text{\AA}$. Wing emission on the red side may exist. The spectrum may suffer from a neighboring continuum source.

IB12-30834 $z = 4.11$, $EW_{\text{rest}} \approx 360\text{\AA}$, $\Delta V \approx 430\text{ km s}^{-1}$. The lower-limit of EW is $\approx 240\text{\AA}$. The line profile is quite simple (nearly Gaussian), and the velocity width is relatively small.

IB12-48320 $z = 4.04$, $EW_{\text{rest}} \approx 320$, $\Delta V \approx 320\text{ km s}^{-1}$. The lower limit of the EW is $\approx 200\text{\AA}$. A relatively strong residual of sky subtraction remains on the red side at $\approx 6145\text{\AA}$. The line profile may suffer from a weak sky emission line here.

IB12-58572 $z = 4.04$, $EW_{\text{rest}} \approx 210\text{\AA}$, $\Delta V \approx 400\text{ km s}^{-1}$. The lower limit of the EW does not exceed 200\AA . This object was categorized as a continuum-compact source in appendix 2.

IB12-81981 $z = 4.12$, $EW_{\text{rest}} \approx 500\text{\AA}$, $\Delta V \approx 380\text{ km s}^{-1}$. The lower limit of the EW is $\approx 260\text{\AA}$. The profile shows asymmetry, but no significant wing emission can be found. The red side suffers from relatively strong sky emission lines at $\approx 6235\text{\AA}$ and 6260\AA , and several weak ones.

IB13-104299 $z = 4.42$, $EW_{\text{rest}} \approx 300\text{\AA}$, $\Delta V \approx 260\text{ km s}^{-1}$. The lower-limit of EW does not exceed 200\AA . The spectrum may suffer from several sky emission lines at $\approx 6560, 6580$, and 6600\AA . The photometry may suffer from a neighboring continuum source.

Table 1. Photometric properties of the VIMOS spectroscopic sample

Object ID	α (J2000) ^a	δ	band	Ly α mag(2'')	mag(auto)	Continuum band	mag(2'')
IB08-86220	2:18:28.34	-5:18:12.2	IA527	25.76	25.40	<i>R</i>	26.51 ^c
IB10-17108	2:16:58.05	-5:34:19.2	IA574	25.07	24.83	<i>R</i>	25.65 ^c
IB10-32162	2:16:56.90	-5:30:29.7	IA574	25.22	24.90	<i>R</i>	25.98 ^c
IB10-54185	2:17:59.49	-5:25:07.5	IA574	25.61	25.13	<i>R</i>	26.44 ^c
IB10-90651	2:17:43.35	-5:16:12.4	IA574	25.84	25.50	<i>R</i>	27.75 ^f
IB11-59167	2:17:10.21	-5:23:47.5	IA598	25.80	25.54	<i>i'</i>	27.59 ^f
IB11-80344	2:17:44.7	-5:18:15.3	IA598	25.53	25.24	<i>i'</i>	27.03 ^f
IB11-89537	2:17:45.3	-5:15:53.6	IA598	25.80	25.52	<i>i'</i>	27.59 ^f
IB12-21989	2:17:13.35	-5:32:56.6	IA624	25.71	25.06	<i>i'</i>	25.88 ^c
IB12-30834	2:17:55.98	-5:30:53.4	IA624	25.82	25.71	<i>i'</i>	27.09 ^f
IB12-48320	2:16:55.89	-5:26:37.1	IA624	25.82	25.35	<i>i'</i>	27.35 ^f
IB12-58572	2:17:49.10	-5:24:11.6	IA624	25.97	25.32	<i>i'</i>	26.82 ^c
IB12-71781	2:17:38.96	-5:20:58.1	IA624	25.96	25.67	<i>i'</i>	26.77 ^c
IB12-81981	2:18:14.72	-5:18:32.5	IA624	25.65	25.27	<i>i'</i>	27.84 ^f
IB13-96047	2:18:13.33	-5:15:05.4	IA651	25.80	25.16	<i>i'</i>	25.97 ^c
IB13-104299	2:18:21.09	-5:13:25.2	IA651	25.87	25.48	<i>i'</i>	27.45 ^f
IB14-47257	2:18: 1.96	-5:25:25.3	IA679	25.93	25.14	<i>i'</i>	26.29 ^c
IB14-52102	2:18:00.12	-5:24:10.6	IA679	25.39	25.15	<i>i'</i>	26.33 ^c

^aCoordinates are based on SXDS version 1 astrometry.

^cContinuum-compact objects: objects which can be regarded as point-sources.

^fContinuum-faint objects: objects which are fainter than 3σ in continuum.

Table 2. Spectral properties

Object ID	λ_c^a [Å]	z	$F(\text{Ly}\alpha)^b$ [10^{-17} ergs cm^{-2} s^{-1}]	$L(\text{Ly}\alpha)$ [10^{42} ergs s^{-1}]	ΔV (FWHM) [km s^{-1}]	EW_{rest} [Å]	wing
IB08-86220	5234	3.31	3.3(1.9) \pm 0.3	3.3 \pm 0.5	423 ⁺⁵⁵ ₋₂₀	121 ⁺³⁴ ₋₂₅	-
IB10-17108	5824	3.79	7.6(4.2) \pm 0.7	10 \pm 2	492 ⁺⁶⁰ ₋₂₁	112 ⁺¹⁹ ₋₁₇	red
IB10-32162	5761	3.74	7.4(3.6) \pm 0.6	9.7 \pm 1.7	614 ⁺⁵⁵ ₋₃₁	149 ⁺²⁹ ₋₂₄	red
IB10-54185	5864	3.82	4.2(2.1) \pm 0.4	6.5 \pm 1.3	295 ⁺²¹ ₋₅₃	128 ⁺³⁵ ₋₂₇	red
IB10-90651	5691	3.68	8.3(4.4) \pm 1.9	11 \pm 2	573 ⁺⁴⁴ ₋₁₇₆	867 ⁺¹¹¹⁰ ₋₄₁₁	red
IB11-59167	6006	3.94	2.2(1.2) \pm 0.3	3.4 \pm 0.8	273 ⁺¹⁵ ₋₄₇	265 ⁺⁴³⁴ ₋₁₁₇	-
IB11-80344	5950	3.89	7.9(3.5) \pm 0.8	11 \pm 3	736 ⁺⁶³ ₋₆₀	569 ⁺³⁸⁷ ₋₁₈₉	-
IB11-89537	6115	4.03	5.3(2.9) \pm 0.5	8.4 \pm 1.4	555 ⁺⁸⁸ ₋₅₀	458 ⁺⁴⁰² ₋₁₆₄	-
IB12-21989	6212	4.11	7.7(3.7) \pm 0.7	13 \pm 2	454 ⁺⁵⁶ ₋₉₇	184 ⁺⁴³ ₋₃₄	-
IB12-30834	6217	4.11	4.9(2.6) \pm 0.5	8.0 \pm 1.4	434 ⁺²⁸ ₋₄₄	357 ⁺²⁵⁵ ₋₁₁₉	-
IB12-48320	6124	4.04	3.4(1.5) \pm 0.4	5.3 \pm 1.2	320 ⁺⁵⁴ ₋₈₀	318 ⁺³³³ ₋₁₁₈	-
IB12-58572	6129	4.04	3.6(1.3) \pm 0.5	5.7 \pm 2.0	398 ⁺⁶⁰ ₋₂₂	208 ⁺¹²³ ₋₆₆	-
IB12-71781	6208	4.11	2.5(1.4) \pm 0.6	4.1 \pm 1.8	291 ⁺⁶⁷ ₋₆₁	134 ⁺⁹⁵ ₋₅₅	-
IB12-81981	6224	4.12	3.4(1.9) \pm 0.4	5.7 \pm 1.1	379 ⁺³² ₋₅₆	500 ⁺¹⁴⁹⁷ ₋₂₄₀	-
IB13-96047	6592	4.27	5.4(2.0) \pm 0.5	10 \pm 3	354 ⁺³⁹ ₋₅₇	135 ⁺³⁴ ₋₂₆	-
IB13-104299	6410	4.42	3.2(2.0) \pm 0.4	5.7 \pm 1.2	259 ⁺²³ ₋₁₆	303 ⁺³⁹³ ₋₁₂₉	-
IB14-47257	6878	4.66	5.6(2.0) \pm 0.8	13 \pm 5	325 ⁺⁸⁴ ₋₃₁	177 ⁺⁶⁶ ₋₄₇	-
IB14-52102	6647	4.47	4.5(2.5) \pm 0.3	9.0 \pm 1.2	353 ⁺⁵⁶ ₋₃₆	152 ⁺⁴⁷ ₋₃₃	red

^aWavelength of the line center.

^bThe values before slit-loss-correction are shown in the parentheses.

Table 3. 1σ flux limits in X-ray

Object ID	z	C.R.L ^a [counts s ⁻¹]	$(N_{\text{H}} = 10^{23}\text{cm}^{-2})$		$(N_{\text{H}} = 10^{24}\text{cm}^{-2})$	
			F_{2-10}^{b} [ergs cm ⁻² s ⁻¹]	L_{2-10}^{c} [ergs s ⁻¹]	F_{2-10}^{b} [ergs cm ⁻² s ⁻¹]	L_{2-10}^{c} [ergs s ⁻¹]
IB08-86220	3.31	4.42×10^{-4}	1.18×10^{-15}	1.45×10^{45}	4.73×10^{-15}	5.83×10^{45}
IB10-17108	3.79	1.40×10^{-3}	3.30×10^{-15}	5.62×10^{45}	1.19×10^{-14}	2.03×10^{46}
IB10-32162	3.74	6.3×10^{-4}	1.51×10^{-15}	2.49×10^{45}	5.51×10^{-15}	9.09×10^{45}
IB10-54185	3.82	6.67×10^{-4}	1.57×10^{-15}	2.72×10^{45}	5.63×10^{-15}	9.76×10^{45}
IB10-90651	3.68	4.46×10^{-4}	1.08×10^{-15}	1.71×10^{45}	4.00×10^{-15}	6.37×10^{45}
IB11-59167	3.94	3.31×10^{-4}	7.63×10^{-16}	1.42×10^{45}	2.66×10^{-15}	4.96×10^{45}
IB11-80344	3.89	4.51×10^{-4}	1.05×10^{-15}	1.90×10^{45}	3.70×10^{-15}	6.70×10^{45}
IB11-89537	4.03	4.43×10^{-4}	1.00×10^{-15}	1.97×10^{45}	3.43×10^{-15}	6.75×10^{45}
IB12-21989	4.11	7.55×10^{-4}	1.68×10^{-15}	3.47×10^{45}	5.67×10^{-15}	1.17×10^{46}
IB12-30834	4.11	1.60×10^{-3}	3.58×10^{-15}	7.38×10^{45}	1.21×10^{-14}	2.50×10^{46}
IB12-48320	4.04	5.97×10^{-4}	1.35×10^{-15}	2.67×10^{45}	4.61×10^{-15}	9.13×10^{45}
IB12-58572	4.04	5.27×10^{-4}	1.19×10^{-15}	2.35×10^{45}	4.07×10^{-15}	8.06×10^{45}
IB12-71781	4.11	3.98×10^{-4}	8.89×10^{-16}	1.83×10^{45}	2.99×10^{-15}	6.16×10^{45}
IB12-81981	4.12	6.28×10^{-4}	1.40×10^{-15}	2.90×10^{45}	4.70×10^{-15}	9.75×10^{45}
IB13-96047	4.27	7.15×10^{-4}	1.55×10^{-15}	3.50×10^{45}	5.06×10^{-15}	1.14×10^{46}
IB13-104299	4.42	6.47×10^{-4}	1.37×10^{-15}	3.36×10^{45}	4.34×10^{-15}	1.06×10^{46}
IB14-47257	4.66	7.18×10^{-4}	1.48×10^{-15}	3.80×10^{45}	4.52×10^{-15}	1.25×10^{46}
IB14-52102	4.47	6.6×10^{-4}	1.39×10^{-15}	3.49×10^{45}	4.35×10^{-15}	1.09×10^{46}

^aCount rate limits in the observed-frame 0.5–4.5 keV.

^bFlux limits in the rest-frame 2–10 keV.

^cLuminosity limits in the rest-frame 2–10 keV.

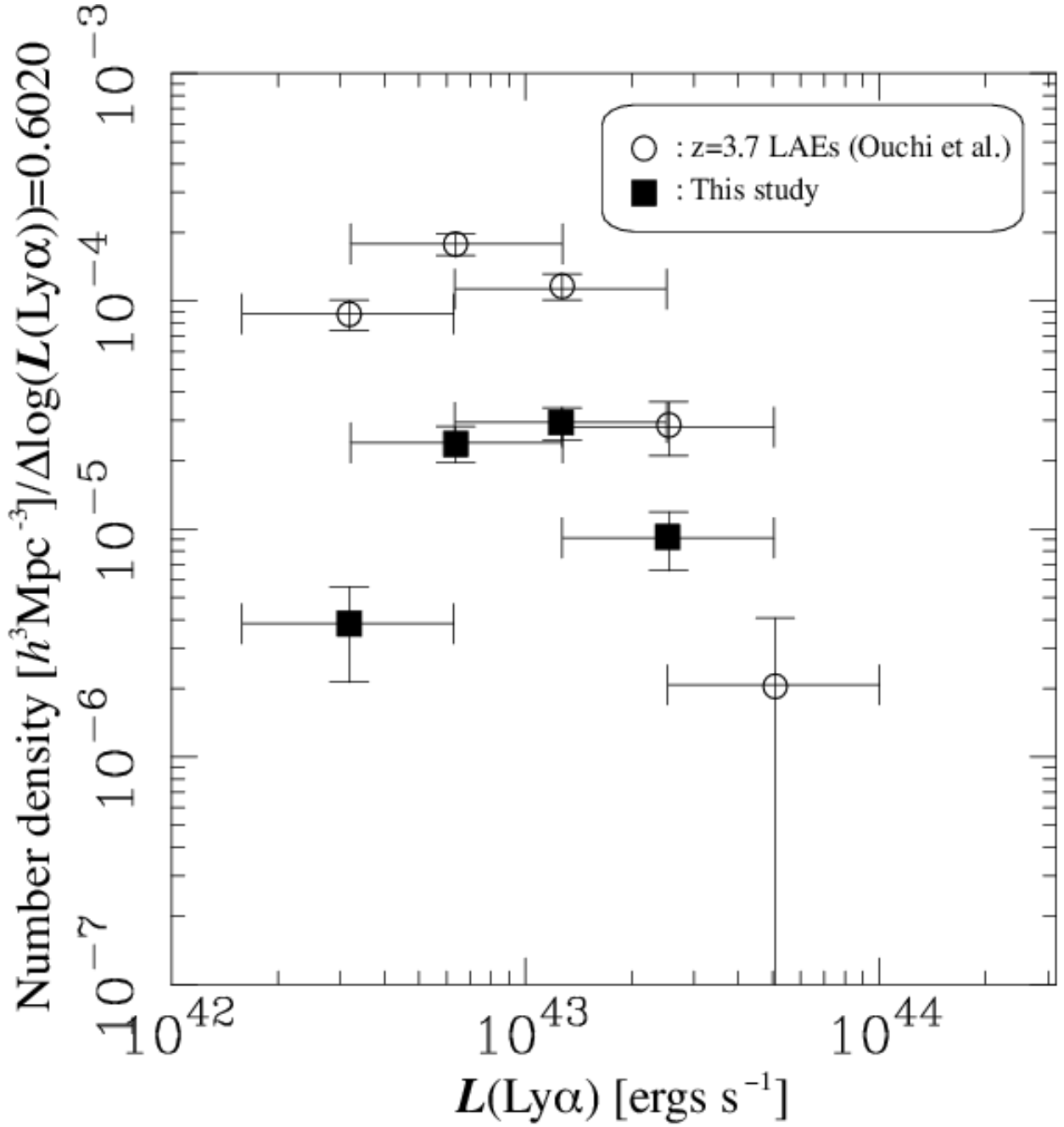


Fig. 1.— Luminosity functions (LFs) of our sample (filled squares) and a sample of normal LAEs at $z \simeq 3.7$ by Ouchi et al. (open circles). The vertical error bars show the Poisson errors, and the horizontal error bars represent the size of the luminosity bins.

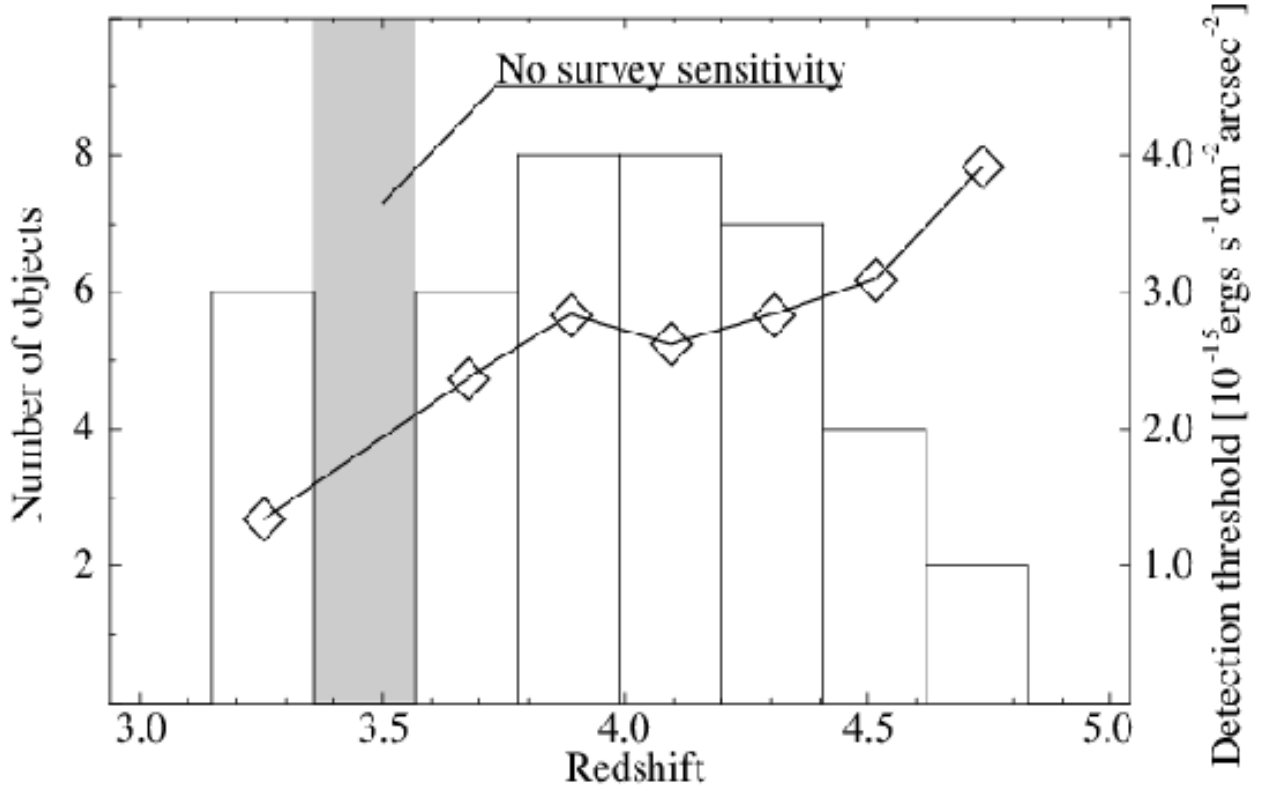


Fig. 2.— Redshift distribution of extended Ly α sources. The histogram shows the redshift distribution of our photometric sample of 41 extended Ly α sources, based on coarse redshift information obtained from the IA imaging (redshift resolution $\Delta z \sim 0.2$). The open diamonds show the detection limit (2σ) for each IA band in units of rest-frame surface brightness (right axis).

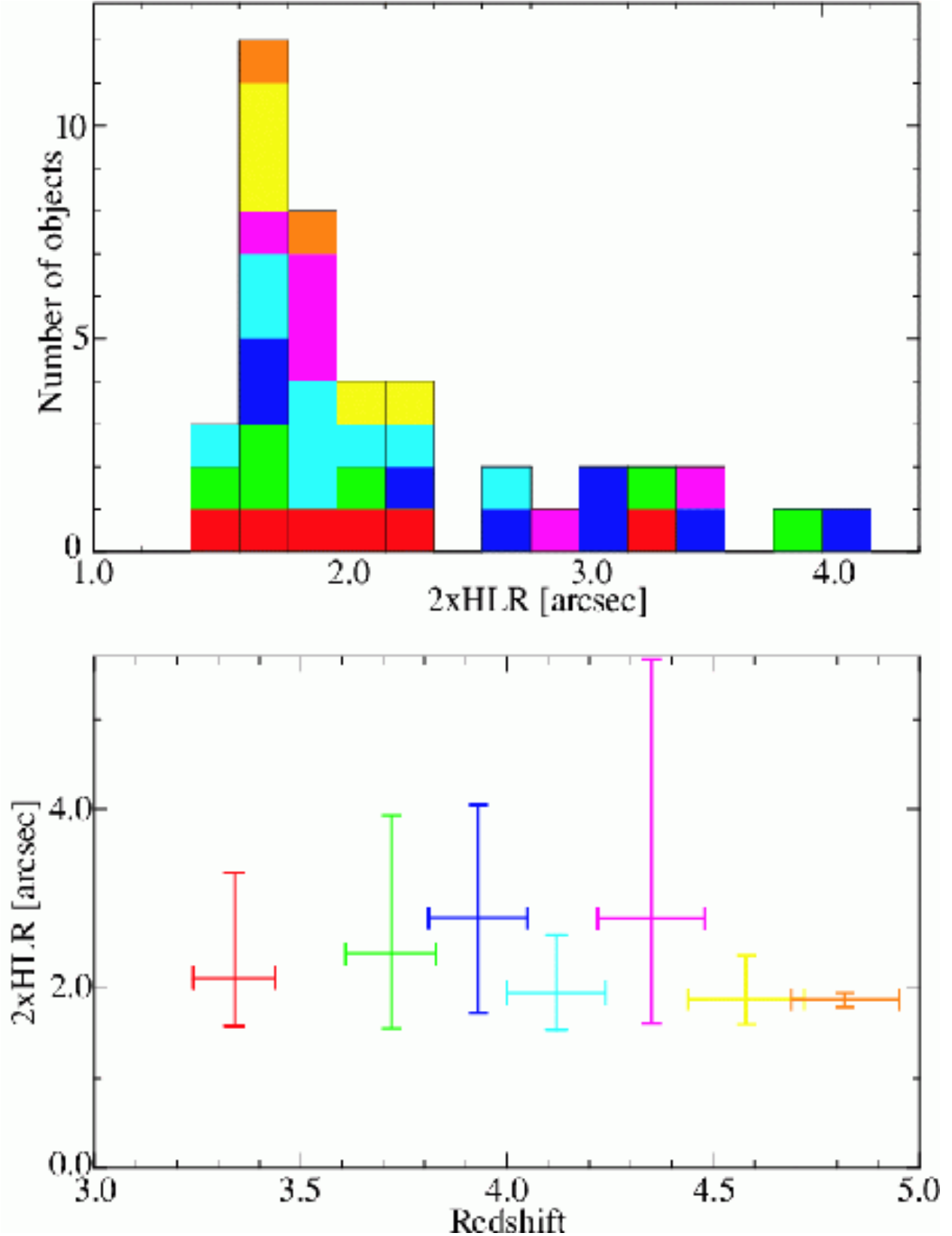
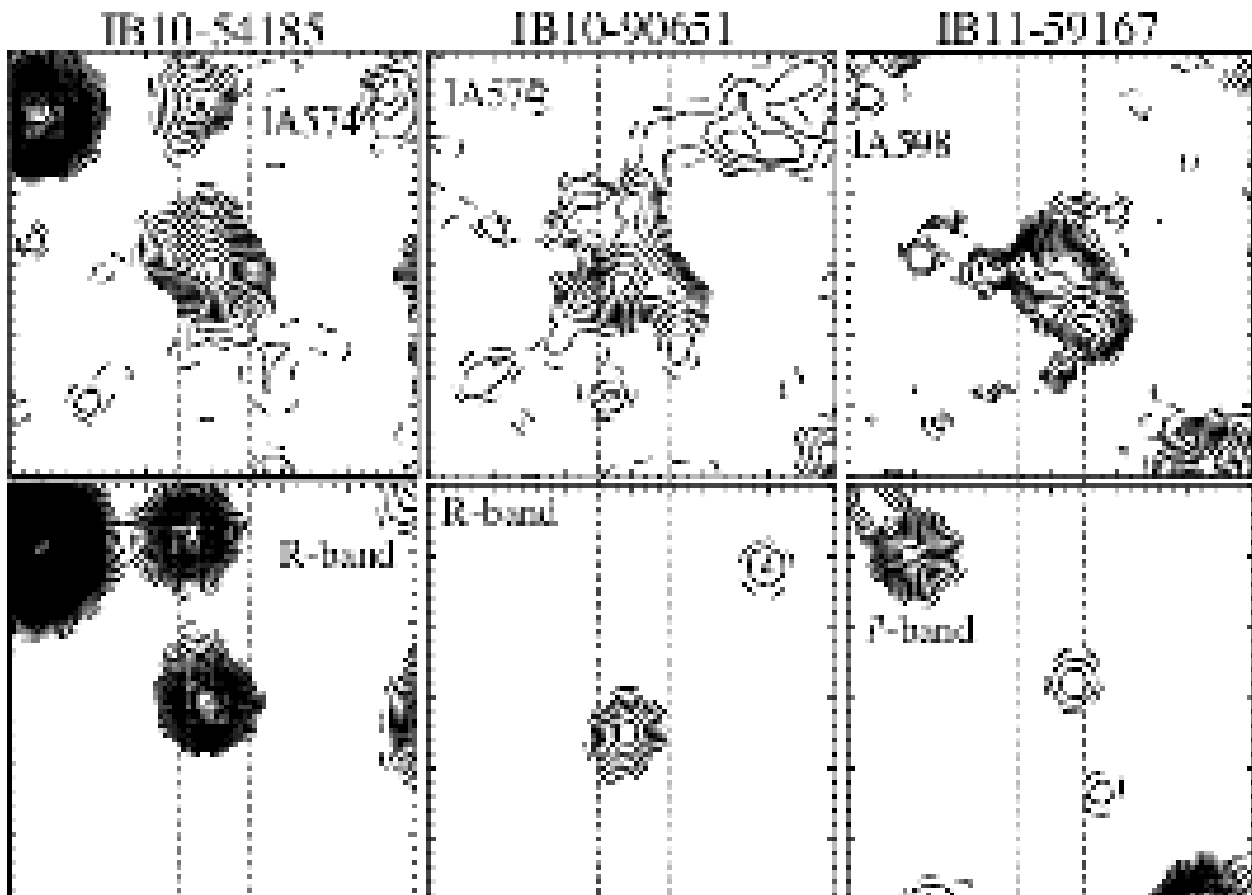
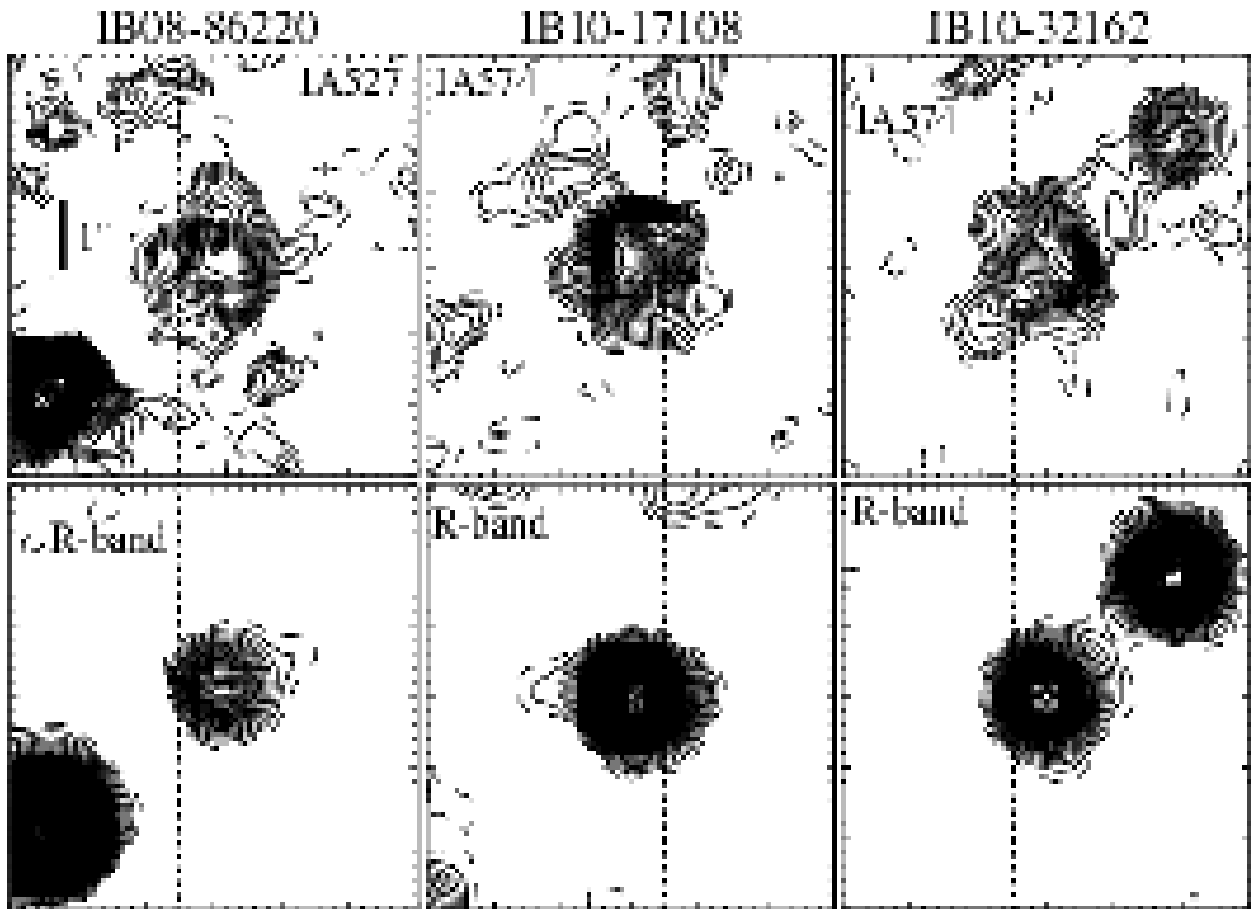
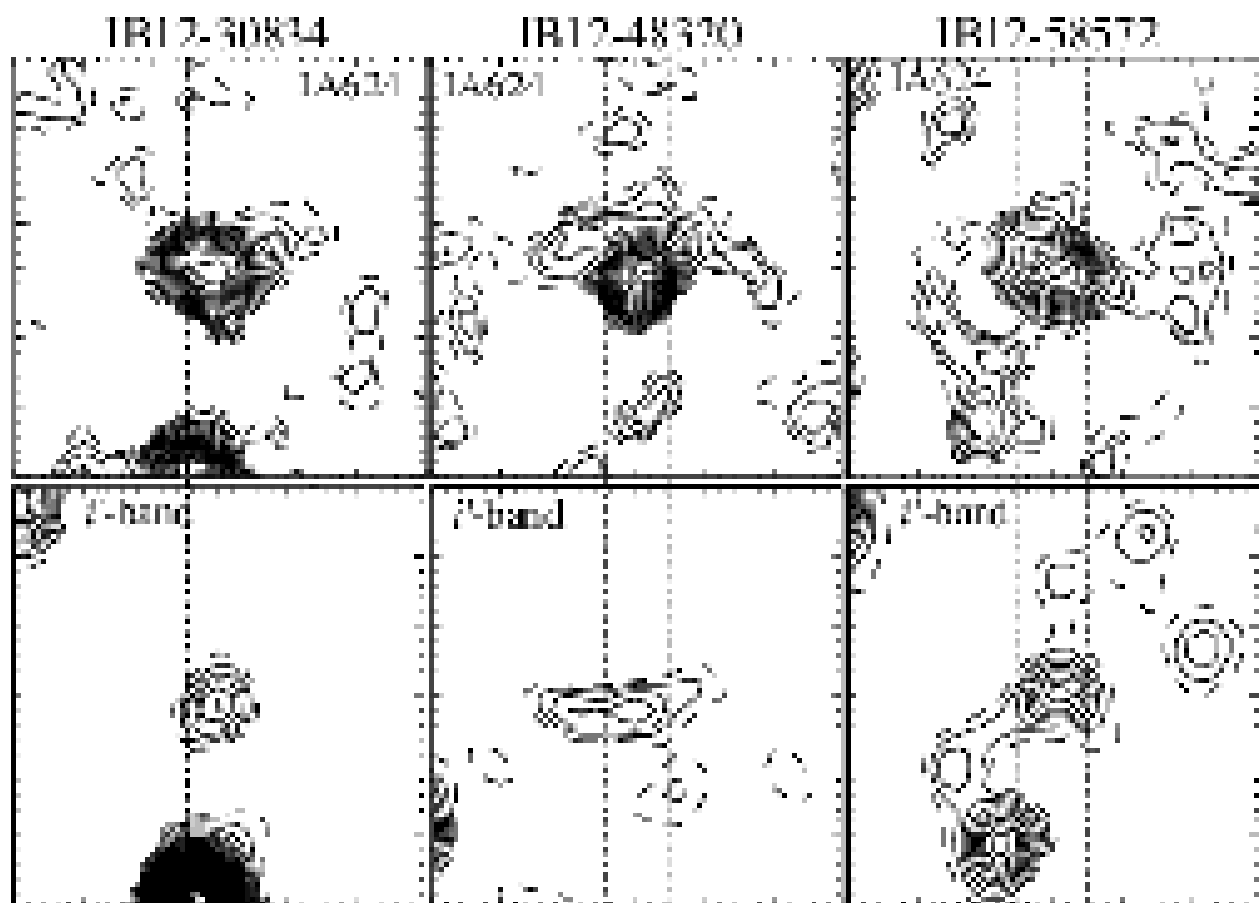
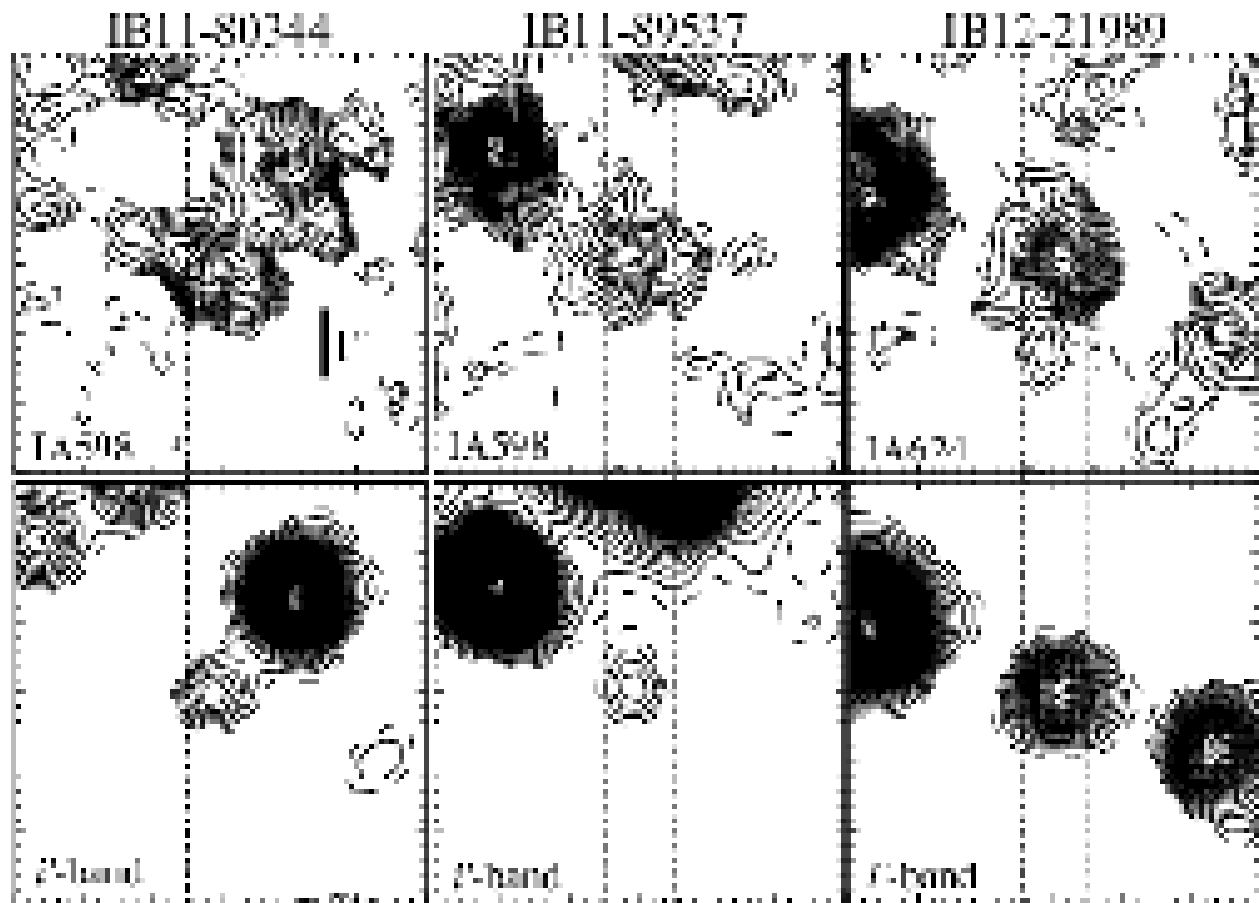
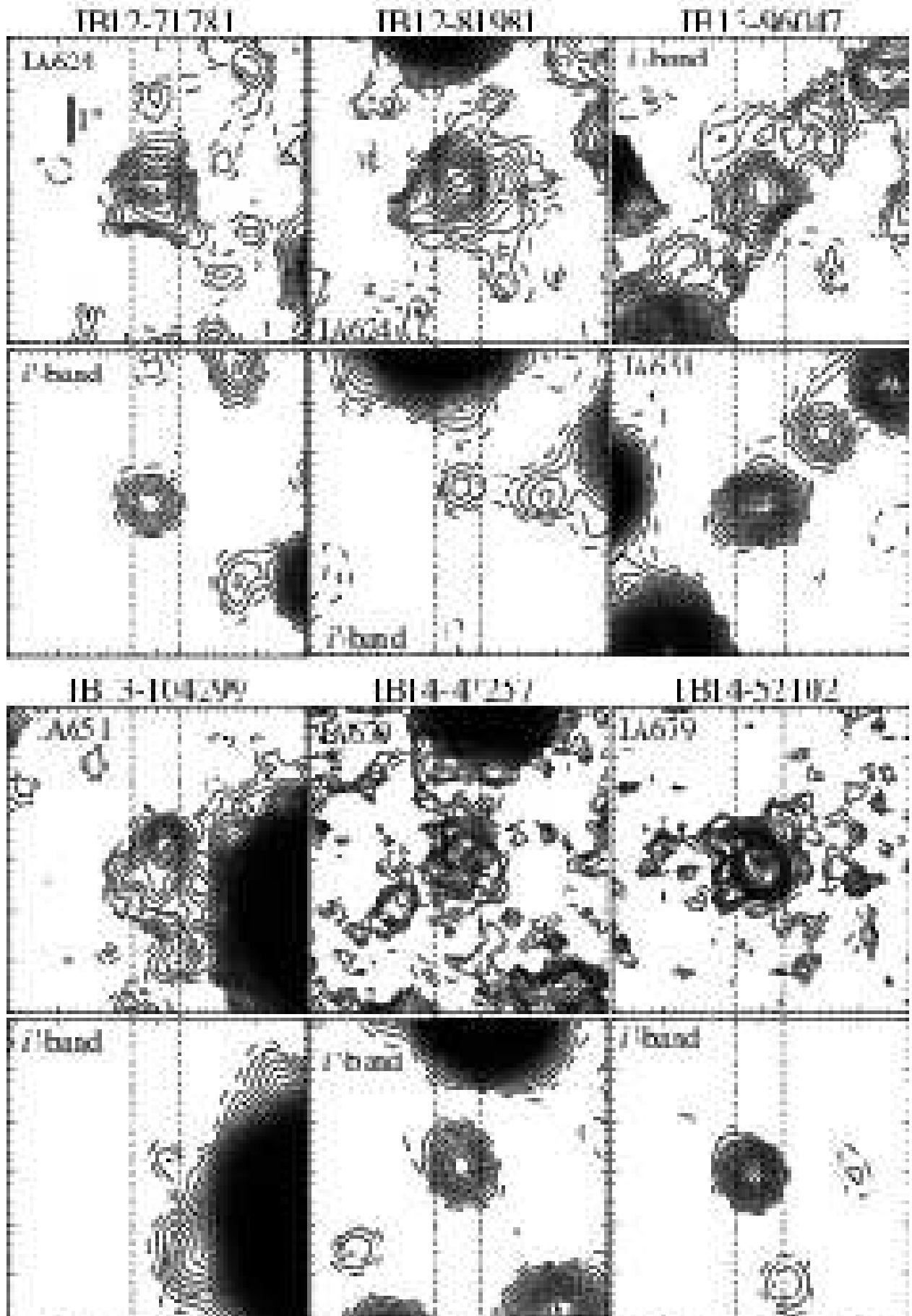


Fig. 3.— Size distribution of the photometric sample of 41 extended Ly α sources. The top panel is a histogram of the size defined by twice the half-light-radius (HLR). The bottom panel shows the size as a function of (roughly estimated) redshift. For both panels, colors correspond to the bands where we detected the Ly α emission. In the bottom panel, the horizontal error bars indicate the







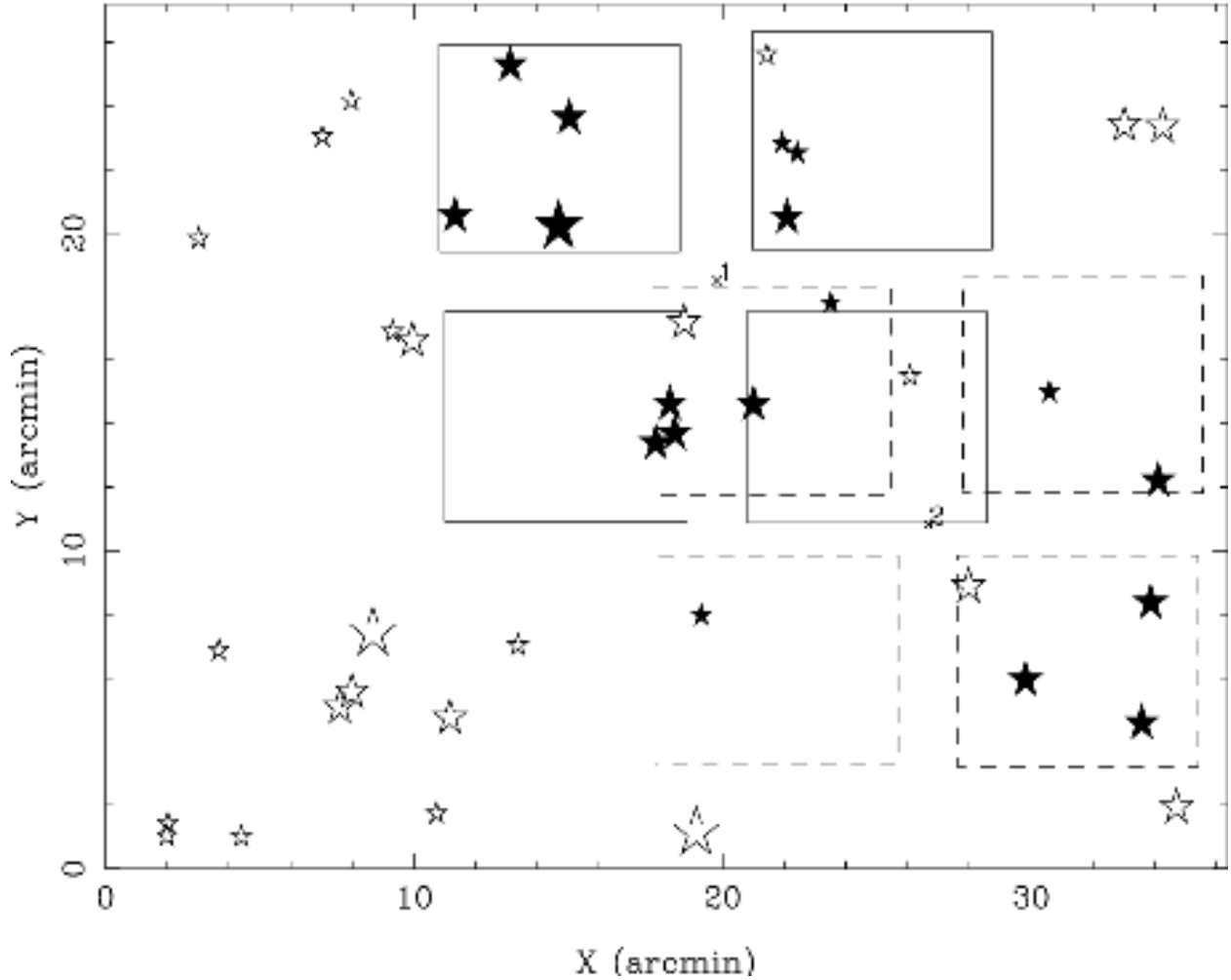


Fig. 5.— Sky distribution of our objects. The solid and dashed rectangles show the two MOS fields of the VIMOS spectroscopy. The 41 objects in the photometric sample are shown in stars, and the 18 objects in the VIMOS sample are shown in filled symbols. The large symbols represent objects brighter than 25.5 mag (AB) in the IA bands with large IA-excess ($\text{Cont} - \text{IA} > 2.0$ mag) The medium large symbols are objects brighter than 25.5 mag in the IA bands.

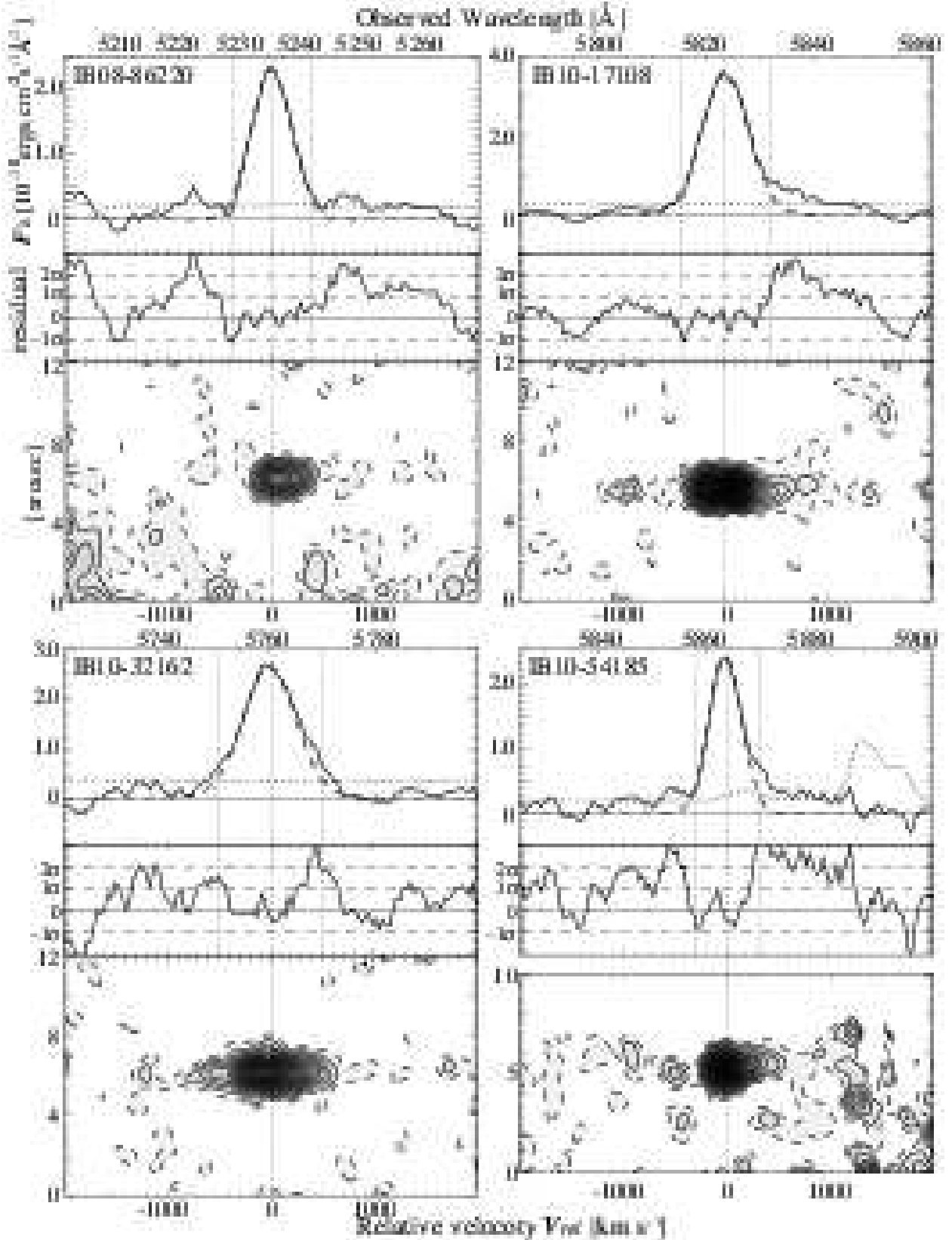


Fig. 6.— Spectra taken with VIMOS. For each object, three panels show line profile, residual of Gaussian fitting, and two-dimensional spectrum (from top to bottom). On the top panel, the solid curve shows line profile, the dotted curve shows sky spectrum scaled to 1/100, and the vertical dotted lines show central wavelength and $\pm 1\sigma$ of the Gaussian function fitted to the line profile.

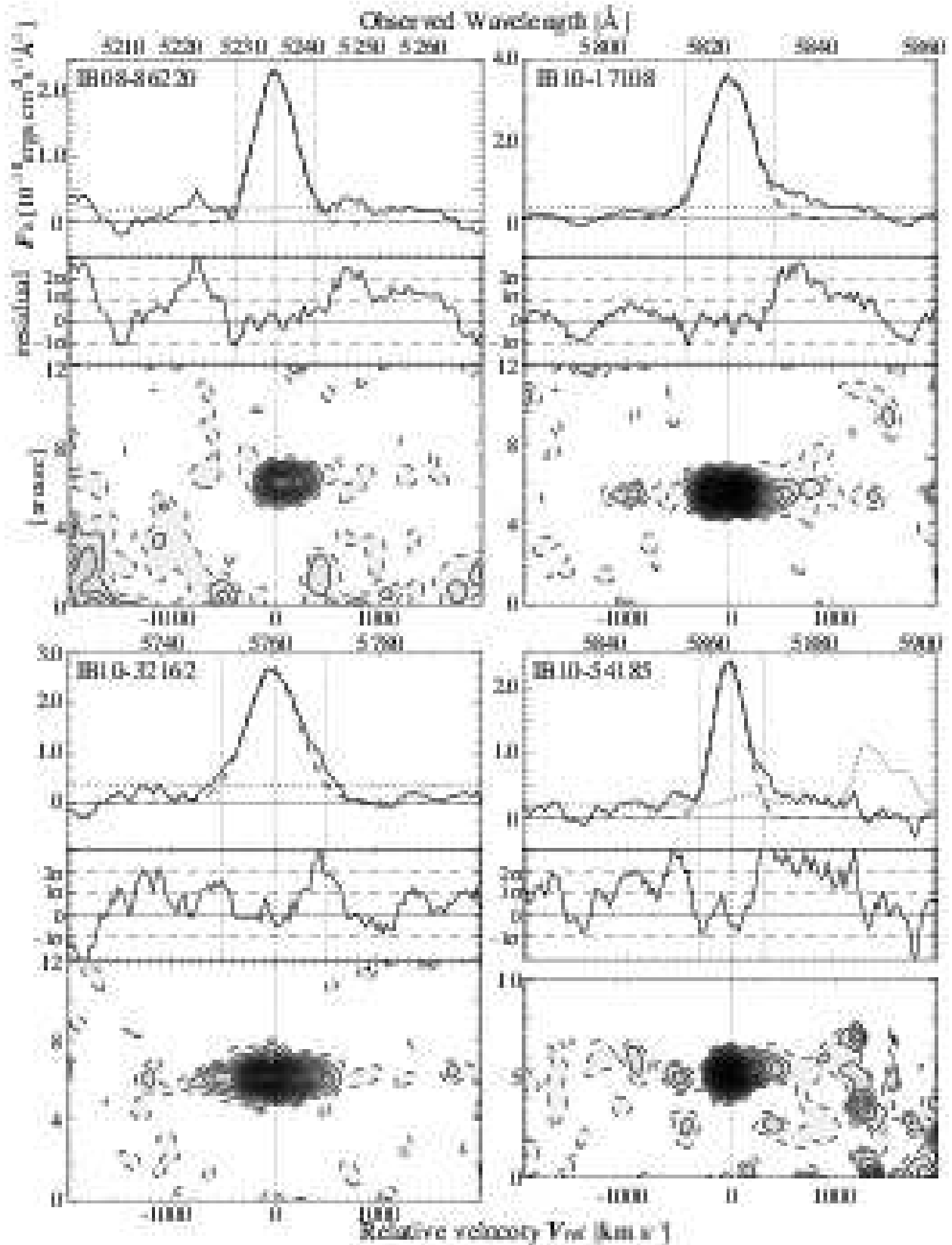


Fig. 6.— Spectra taken with VIMOS. (Continued)

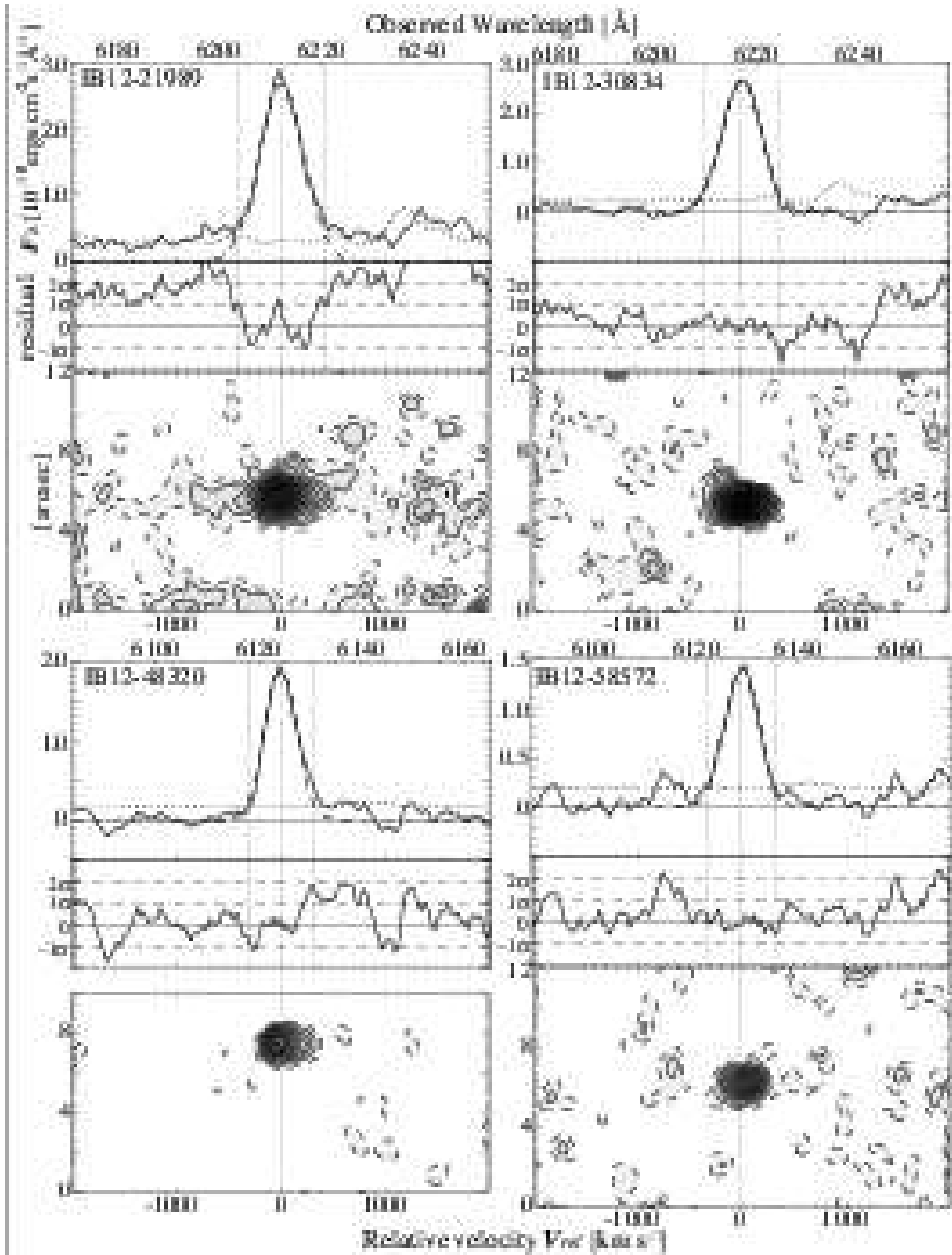


Fig. 6.— Spectra taken with VIMOS. (Continued)

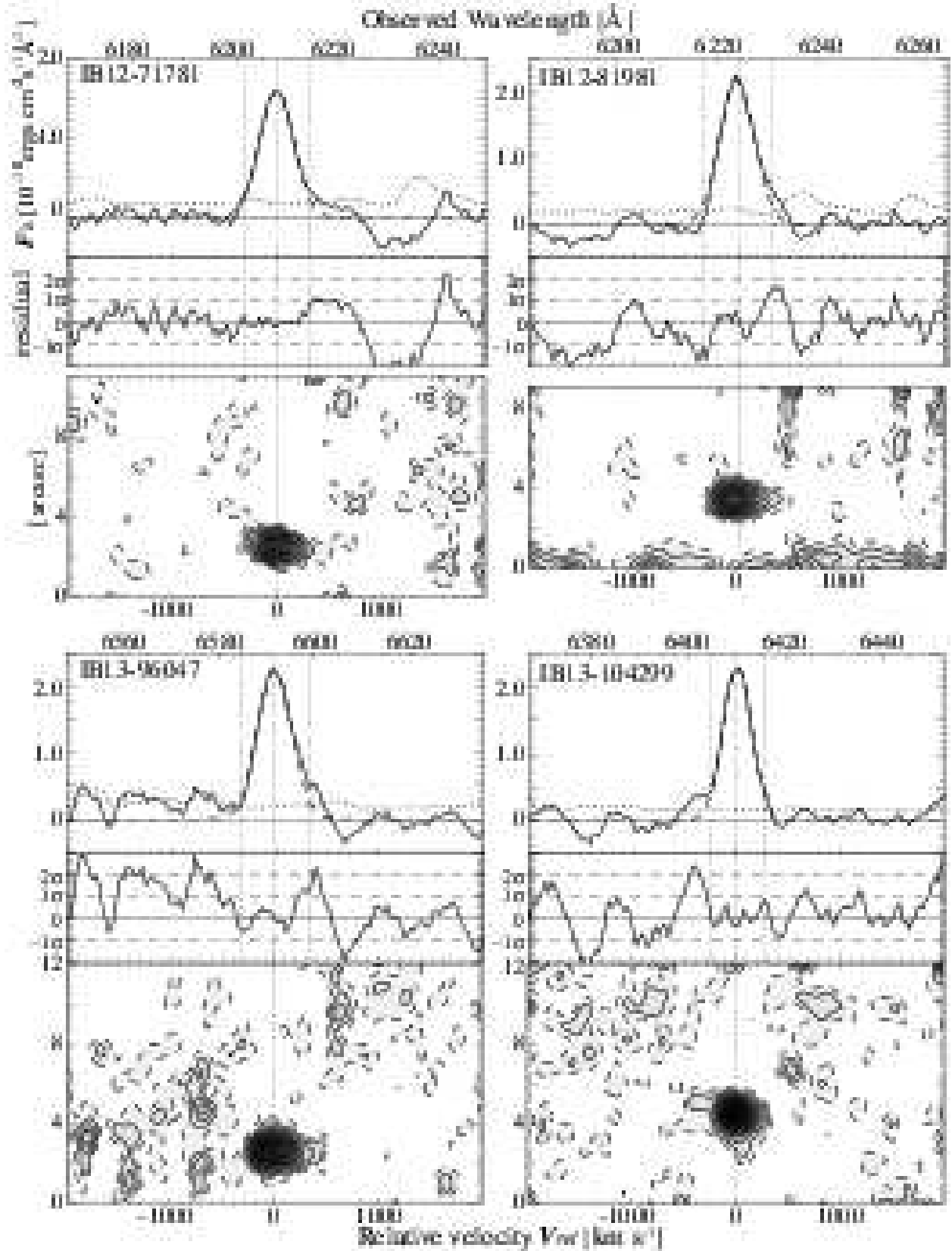


Fig. 6.— Spectra taken with VIMOS (Continued)

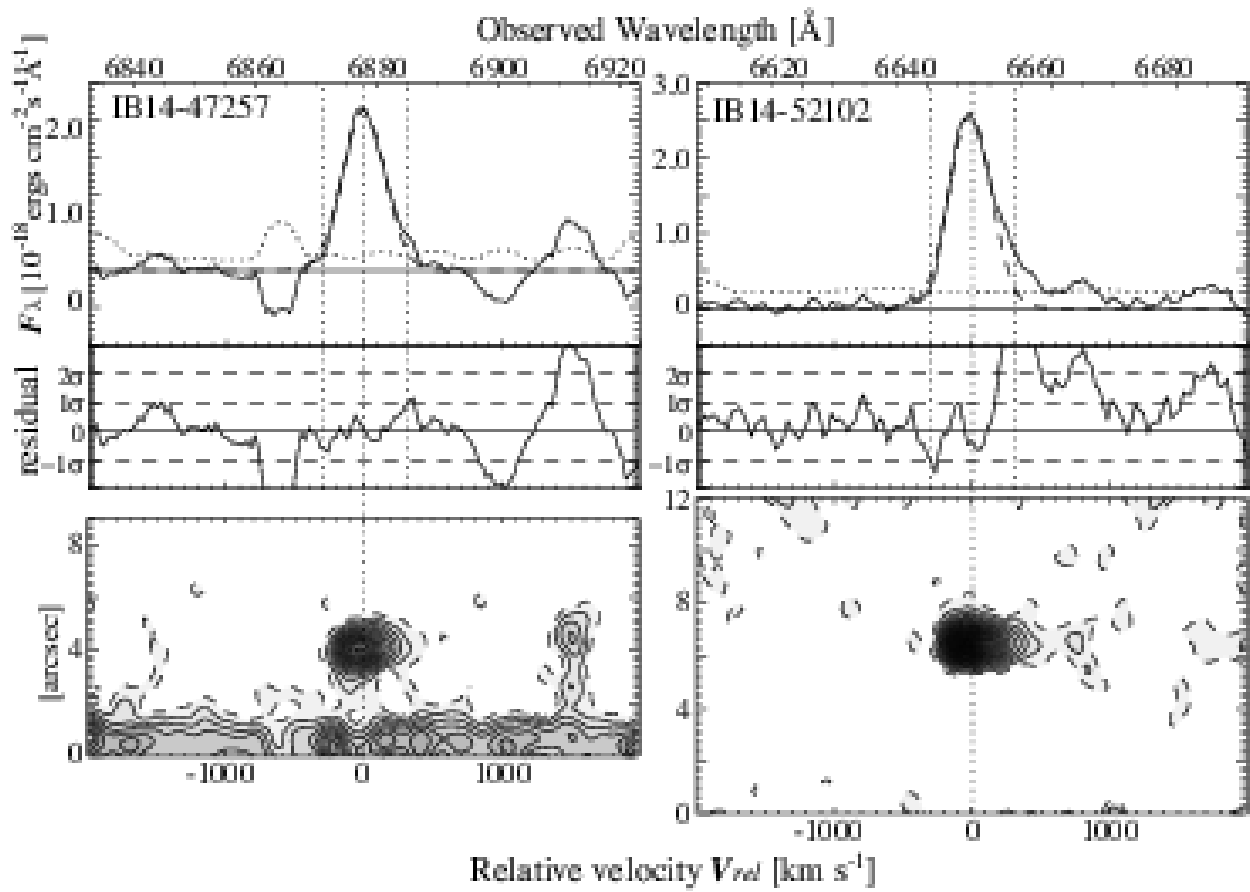


Fig. 6.— Spectra taken with VIMOS (Continued)

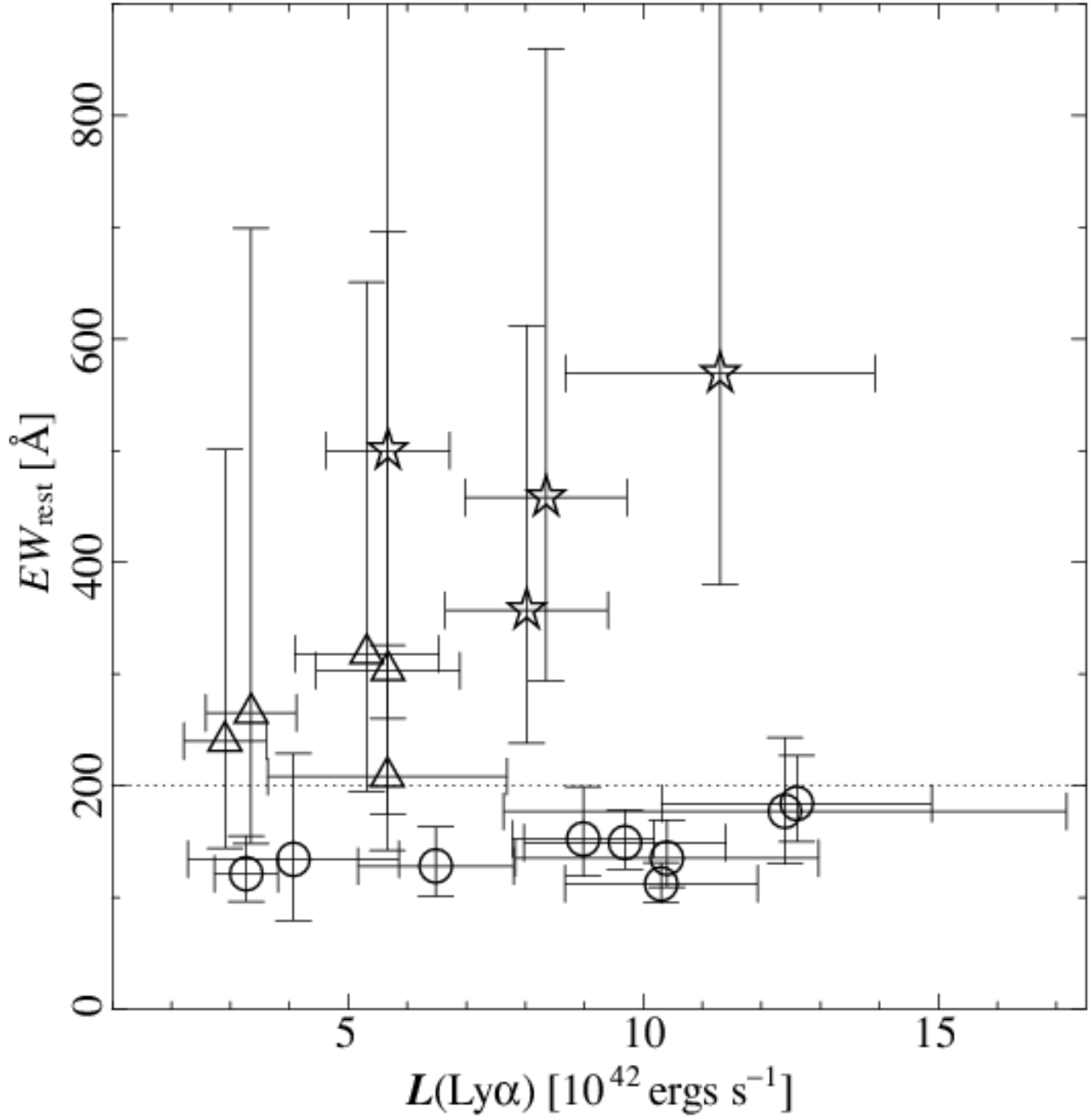


Fig. 7.— Equivalent width of the Ly α line as a function of the Ly α line luminosity. The horizontal dotted line corresponds to 200 \AA . Objects marked with open stars have EWs whose lower limits exceed 200 \AA . Open triangles show objects with EWs larger than 200 \AA , but with lower limits below 200 \AA . The remaining objects, which have EWs less than 200 \AA , are marked with open circles.

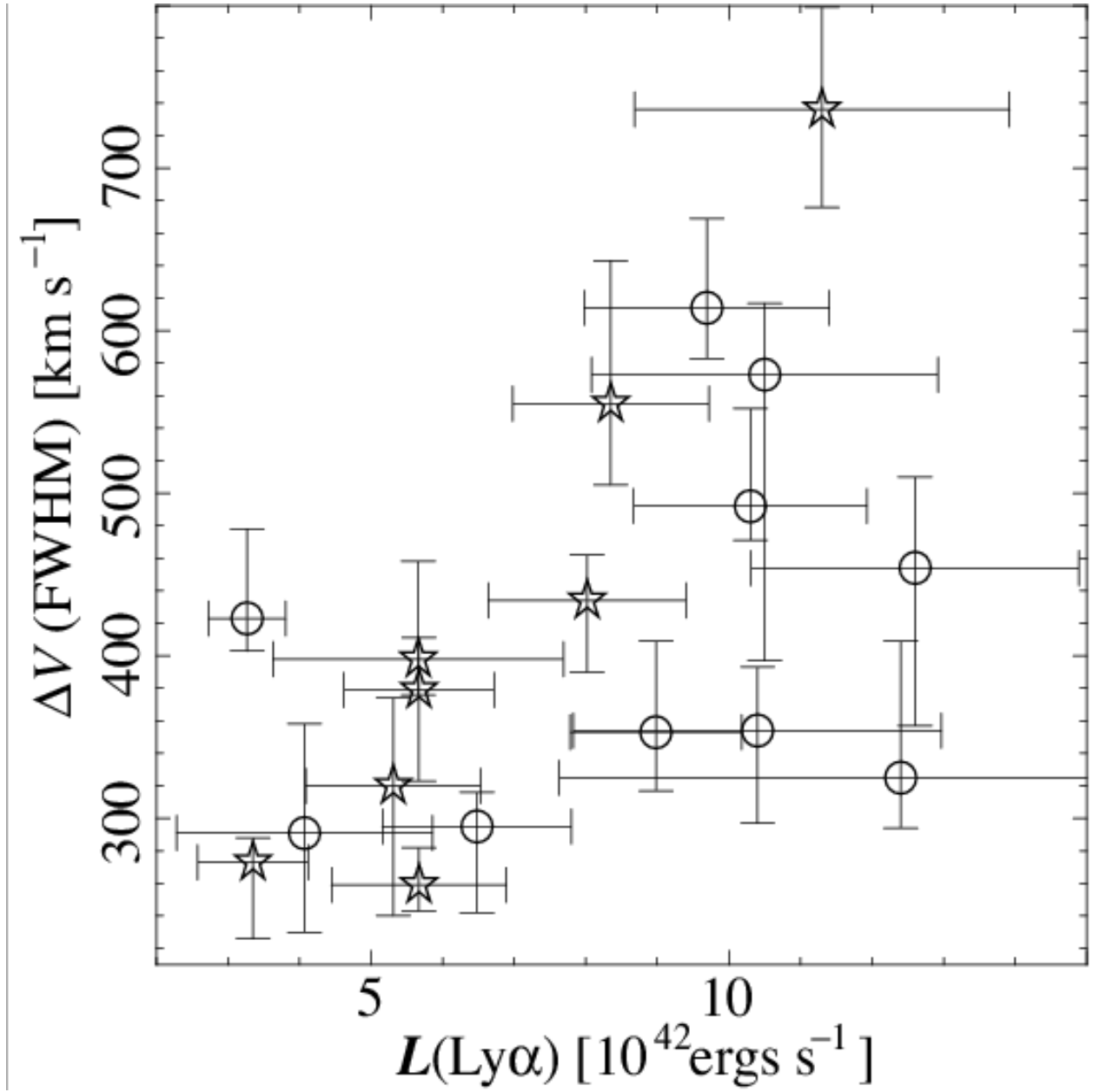


Fig. 8.— Velocity width (FWHM) as a function of the Ly α line luminosity. Objects with large EWs exceeding 200Å are plotted with the open stars.